

The bright-end galaxy candidates at $z \sim 9$ from 79 independent *HST* fields

T. Morishita¹, M. Trenti^{2,3}, M. Stiavelli¹, L. D. Bradley¹, D. Coe¹, P. A. Oesch⁴, C. A. Mason^{5,6,10}, J. S. Bridge⁷, B. W. Holwerda⁷,
R. C. Livermore^{2,3}, B. Salmon¹, K. B. Schmidt⁸, J. M. Shull⁹, T. Treu⁵

¹Space Telescope Science Institute, 3700 San Martin Drive, Baltimore, MD 21218, USA; tmorishita@stsci.edu

²School of Physics, University of Melbourne, VIC 3010, Australia

³ARC Centre of Excellence for All-Sky Astrophysics in 3 Dimensions, Australia

⁴Geneva Observatory, University of Geneva, Ch. des Maillettes 51, 1290 Versoix, Switzerland

⁵Department of Physics and Astronomy, UCLA, 430 Portola Plaza, Los Angeles, CA 90095-1547, USA

⁶Harvard-Smithsonian Center for Astrophysics, 60 Garden St, Cambridge, MA 02138, USA

⁷Department of Physics and Astronomy, 102 Natural Science Building, University of Louisville, Louisville, KY 40292, USA

⁸Leibniz-Institut für Astrophysik Potsdam, An der Sternwarte 16, D-14482 Potsdam, Germany

⁹CASA, Department of Astrophysical and Planetary Science, University of Colorado, Boulder, CO 80309, USA and

¹⁰Hubble Fellow

Accepted to the *Astrophysical Journal*

Abstract

We present a full data analysis of the pure-parallel *Hubble Space Telescope* (*HST*) imaging observations in the Brightest of Reionizing Galaxies Survey (BoRG[z9]) in Cycle 22. The medium-deep exposures with five *HST*/WFC3IR+UVIS filter bands from 79 independent sightlines (~ 370 arcmin²) provide the least biased determination of number density for $z \gtrsim 9$ bright galaxies against cosmic variance. After a strict two-step selection for candidate galaxies, including dropout color and photometric redshift analyses, and revision of previous BoRG candidates, we identify one source at $z \sim 10$ and two sources at $z \sim 9$. The $z \sim 10$ candidate shows evidence of line-of-sight lens magnification ($\mu \sim 1.5$), yet it appears surprisingly luminous ($M_{UV} \sim -22.6 \pm 0.3$ mag), making it one of the brightest candidates at $z > 8$ known (~ 0.3 mag brighter than the $z = 8.68$ galaxy EGSY8p7, spectroscopically confirmed by Zitrin and collaborators). For $z \sim 9$ candidates, we include previous data points at fainter magnitudes and find that the data are well fitted by a Schechter luminosity function with $\alpha = -2.1^{+0.3}_{-0.3}$, $M_{UV}^* = -21.0^{+0.7}_{-1.4}$ mag, and $\log \phi^* = -4.2^{+0.6}_{-0.9}$ Mpc⁻³ mag⁻¹, for the first time without fixing any parameters. The inferred cosmic star formation rate density is consistent with unaccelerated evolution from lower redshift.

Key words: cosmology: observations, galaxies: evolution, galaxies: high-redshift

1. Introduction

Cosmic reionization is one of the frontiers of modern astronomy (Planck Collaboration et al. 2014; see also Robertson et al. 2010). Of particular interest is which class of astrophysical objects is primarily responsible for this phenomenon, which is likely to happen at $z \sim 6-9$ (e.g., Fan et al. 2000; Totani et al. 2006; Shull et al. 2012; Treu et al. 2013; Konno et al. 2014; Schmidt et al. 2014; Mason et al. 2018a,b). Determining luminosity functions (LFs) at such an early epoch is therefore a fundamental step in estimating the net contribution from luminous sources, including active galactic nuclei (AGNs) (Fan et al. 2006; Treu et al. 2012; Trenti et al. 2012a; Madau & Dickinson 2014; Bouwens et al. 2015a).

After a decade of effort, it seems likely that galaxies at the faint end of the LF ($M_{UV} \gtrsim -18$ mag) are the key driver in the reionization epoch (Ellis et al. 2013; Schenker et al. 2013; McLure et al. 2013; Oesch et al. 2013; Ono et al. 2013; Atek et al. 2015; Ishigaki et al. 2015; Livermore et al. 2017; Oesch et al. 2018; Ishigaki et al. 2018), though with a non-negligible impact from uncertainties, in particular from lens modeling (e.g., Atek et al. 2018).

On the other hand, quantifying the number density and properties of the brightest galaxies in the early universe still remains an open yet important field, because these objects constrain the overall shape of the LF (Bouwens et al. 2015b; Ono et al. 2018). Furthermore, these massive objects encode information on in-situ star formation at even earlier times and

probe their building blocks (e.g., Stiavelli 2009), which are the key to understanding the objects at $z \lesssim 7$ (e.g., Ouchi et al. 2010; Sobral et al. 2015).

The shape of LFs in the high- z /high-luminosity regime is yet poorly sampled and its whole shape is undetermined, partly suffering from low- z interlopers (e.g., Livermore et al. 2018, Bridge, in preparation). In particular, current observations with the *Hubble Space Telescope* (*HST*) do not resolve the debate on whether the LF should remain Schechter-like, as it is at lower redshift (e.g., Trenti et al. 2010; Jaacks et al. 2012; Finkelstein et al. 2015; Mason et al. 2015b), or become a (double) power law with enhancement at the bright end, due to the differential impact of dust attenuation (e.g., Clay et al. 2015; Finkelstein et al. 2015), AGN feedback (Finlator et al. 2011), and/or mass quenching (Birnboim & Dekel 2003; Peng et al. 2010; Woo et al. 2013).

Legacy field investigations with *HST* have covered a substantial area ($\gtrsim 800$ arcmin² down to ~ 27 mag; Grogin et al. 2011; Koekemoer et al. 2011), and the latest samples are approaching ~ 1000 sources (e.g., Bouwens et al. 2015b). However, at the bright end one concern in addition to the paucity of candidates is the strong clustering of these sources, with bias factor exceeding $b > 8$ (Barone-Nugent et al. 2014). This in turn implies that contiguous fields can be significantly affected by cosmic variance (Trenti & Stiavelli 2008).

The Brightest of the Reionizing Galaxies (BoRG) Hubble Space Telescope survey (Bradley et al. 2012; Trenti et al.

2012b) has been designed specifically to contribute towards an unbiased measurement of the number density of the brightest and most clustered sources at $z \gtrsim 8$, by taking advantage of pure-parallel (random pointing) opportunities to cover a wide area with medium-deep optical and IR imaging (5σ limiting magnitude $m_{AB} \sim 26.5$), over more than 100 independent sightlines so far.

The initial BoRG survey aimed at the bright end of the LF at $z \gtrsim 8$, using four filters on WFC3 (Trenti et al. 2011, 2012b; Bradley et al. 2012; Bernard et al. 2016). Schmidt et al. (2014) explored 350 arcmin² and found 38 *Y*-band dropout candidates with $L \approx L_*$, providing one of the strongest constraints on the shape of the $z \sim 8$ LF. A continuation of the survey, BoRG[z9] (GO13767, PI. M. Trenti), which we present in this study, is optimized for galaxies at higher redshift ($z \gtrsim 9$) with an updated set of five WFC3IR/UVIS filters. Preliminary results from this survey were presented in Calvi et al. (2016, hereafter C16) by using $\sim 1/3$ of the full data, demonstrating the strength of the new strategy.

In this paper, we present the full data set of BoRG[z9]—a collection of 79 independent sightlines (~ 370 arcmin²) down to ~ 27 mag—which is the least biased survey in the early universe in terms of cosmic variance.¹ We base our analysis on the well-studied color selection method presented in C16. We then further constrain the color-selected candidates with additional criteria, which include photometric redshift priors based on a theoretical model as well as follow-up *Spitzer* photometry. Our new selection also updates the candidates found in C16, providing a final set of one candidate at $z \sim 10$ and two at $z \sim 9$, respectively, from all BoRG[z9] fields. Finally, taking into account simulations of source recovery and completeness, and with the inclusion of data for faint galaxies from the literature, we determine the LF at $z \sim 9$ for the first time without fixing any parameters.

Throughout the paper, magnitudes are quoted in the AB system (Oke & Gunn 1983). We assume $\Omega_m = 0.3$, $\Omega_\Lambda = 0.7$, $H_0 = 70$ km s⁻¹ Mpc⁻¹. We refer to the WFC3 filters F350LP, F105W, F125W, F140W, and F160W as O_{350} (optical), Y_{105} , J_{125} , JH_{140} , and H_{160} , respectively.

2. Data and Sample Selection

In the present study, we use the full data set of BoRG[z9], which consists of 79 independent field of views (FoVs) ~ 370 arcmin². These data have been made publicly available as Version 3 of the BoRG survey as fully calibrated and aligned science images.² This analysis includes the data previously studied in C16, which consists of 28 initial FoVs (~ 130 arcmin²). Inclusion of the previous data set allows us to check the consistency and to see if updates made in the present analysis affect the final results.³

2.1. Survey Design

BoRG[z9] is a pure-parallel *HST* imaging survey with five broadband filters spanning from the NUV/optical band of WFC3/UVIS (O_{350}) to near-IR ($Y_{105}/J_{125}/JH_{140}/H_{160}$) of WFC3/IR. Its medium deep exposures (~ 2 -5 ks) in random

sightlines optimize for detecting bright galaxies, and reach typical limiting magnitudes of $m_{5\sigma} \sim 27$ mag measured in an $0.''32$ radius aperture (see Appendix A).

The major update in BoRG[z9] from our previous studies (*HST* Cycles 17 and 19; Trenti et al. 2011, 2012b; Bradley et al. 2012; Schmidt et al. 2014) is the use of a long-pass filter in the optical wavelength range. O_{350} covers $\sim 0.3 \mu\text{m}$ to $1.0 \mu\text{m}$, while many other studies use a single or multiple broadband filters in the optical range. The choice optimizes rejection of contaminants for the selection of $z > 8$ sources.

For our primary science goal, the collection of $J_{125}H_{160}$ and $Y_{105}JH_{140}$ -dropout sources, persistence is of particular concern because of the possibility of introducing an artificial coherent signal into the near-IR bands. In each visit of this program, we therefore arranged the sequence of WFC3/IR filters to minimize the impact. As detector persistence decays over time, with approximate power-law behavior, any saturated target observed in a previous visit most affects the initial part of the pure-parallel orbit. The general strategy therefore is to observe in the dropout filter as early as possible in the orbit, ideally placing the Y_{105} -band first. However, doing so would result in increased time-varying backgrounds from scattered-light Earth glow from helium in the upper atmosphere (caused by a He 10830 Å line; Brammer et al. 2014). Because the intensity of the scattered Earth glow decreases with increasing target angles above the bright Earth limb, we opted to place the Y_{105} observations as the second filter after J_{125} (or sometimes third when the orbit begins with O_{350}) in an orbit. Whenever possible, observations in JH_{140} and H_{160} follow those filters. With this strategy, persistence features are essentially prevented from contaminating the $J_{125}H_{160}$ and $Y_{105}JH_{140}$ -dropout selections.

To ensure good sampling of the IR exposures, we opted for reading every 50 s (SPARS50). While the majority of cosmic rays are rejected by the calibration pipeline, owing to the multiple non-destructive readouts of the WFC3IR detector, a small fraction may survive in the calibrated image. We thus split the total integration in each IR filter into at least two individual exposures. O_{350} exposures obtained with the UVIS CCD are split into more than two sequences (each 450-900 seconds) for optimal cosmic-ray rejection. Our design choices are aimed at maximizing the data quality, though a small price is paid in signal-to-noise ratio (S/N) by increasing the number of individual exposures.

2.2. Data Reduction

We reduced the raw imaging data by using the *HST* pipeline in the standard manner. In addition to running calwf3, processing of O_{350} included a correction for the Charge-Transfer Efficiency effect (CTE19; Noeske et al. 2012; Anderson 2014). For all filters, we also performed a customized extra step to remove residual cosmic rays and/or detector artifacts, such as unflagged hot pixels, by using a Laplacian edge filtering algorithm (LACOSMIC; van Dokkum et al. 2001) that was used for the previous BoRG data reduction (Bradley et al. 2012; Schmidt et al. 2014, see also C16).

The pixel scale is set to 0.08 arcsec/pixel with pixfrac to 0.75, as in C16. Since most of our images are taken without dithering, we use a slightly larger pixel scale than typical non-parallel observations (~ 0.06 arcsec/pixel). The only change from C16 is made in one of the parameters of cosmic-ray detection, where we set cr_threshold to 3σ and 1.5σ (compare 3.9σ and 5σ in C16) for UVIS and IR detectors, respectively,

¹ For example, cosmic variance for our 79 independent FoVs reduces to $\sim 26\%$ of the value for a single contiguous survey with the same area coverage (Trenti & Stiavelli 2008).

² <https://archive.stsci.edu/prepds/borg/>

³ Since we update the source detection parameters from C16, target IDs between the two studies are not identical.

in the LACOSMIC Python package⁴. This significantly reduces the residual cosmic rays compared to the previous data products.

This reduction process generates science and rms maps for the five filter bands, in addition to a combined $JH_{140}+H_{160}$ map for the use of detection images (see below). It is noted that the RMS maps generated by the pipeline have arbitrary infinity values for, e.g., dead pixels and/or those with a cosmic-ray flag. Such an artificial value in fact affected the previous sample selection in C16 (see Section 3.1.1). We replace those values with 0, so that a detection algorithm (i.e. SExtractor; Bertin & Arnouts 1996) ignores them; otherwise it would falsely return infinity values for fluxes in such regions.

The RMS map of each filter band generated by the pipeline is then scaled so that it represents the true uncertainty, including correlated noise (Casertano et al. 2000). To account for this, we follow the scaling method presented by Trenti et al. (2011). Briefly, we measure the median sky in the empty region in each mosaic image by using SExtractor (Bertin & Arnouts 1996) with the same setup parameters as the source detection. Each RMS map is then scaled so that the dispersion in flux of the sky region (f_{aper} , in an aperture of $r = 0.''32$) and its estimated error (e_{aper}) are consistent. The median values of the scale factor are 1.174, 1.195, 1.209, 1.233, 1.708 for H_{160} , JH_{140} , J_{125} , Y_{105} , and O_{350} , respectively, which are consistent with C16. This process also returns limiting magnitudes (i.e. median of f_{aper} in each field), which are used for upper limits of non-detection.

Ten out of the 89 original survey fields are discarded from our final analysis, because they failed in the acquisition of a guide star or are dominated by a number of bright stars. The list of fields is summarized in Appendix A.

The point-spread functions (PSFs) of different filter images are not matched in this study, because it is challenging to accurately measure the PSF in each of our data with relatively shallow exposures. However, as the apparent size of our target galaxies is typically small, in addition to the use of optimized photometry (i.e. isophotal flux; see Section 2.3), the effect is minimal (see also Oesch et al. 2007; Trenti et al. 2012b; Holwerda et al. 2014).

2.3. Detection and Color Selection of Dropout Galaxies

We first detect galaxies using SExtractor in the $JH_{140}+H_{160}$ stacked image. The detection parameters are set as C16—DETECT_MINAREA = 9, NTHRESH = 0.7σ , DEBLEND_NTHRESH = 32, DEBLEND_MINCONT = 0.01. The exception is the convolution size (FWHM of Gaussian) for detection in SExtractor, which is changed from 2 pixels to 5 pixels. This reduces false detection of, e.g., discrete noise at the edge of the detector and residual cosmic rays. The photometry is performed in the dual-imaging mode, based on the $JH_{140}+H_{160}$ detection. With this setup, we detect 73374 objects from all BoRG fields in this study.

We then select those with $S/N_{JH_{140}+H_{160}} > 8$ for robust detection, and with CLASS_STAR < 0.95 to avoid stars. Signal-to-noise ratios are calculated from the measurement and error of the isophotal flux of SExtractor. Compared to other schemes of photometry, the choice flexibly corresponds to source morphology. For example, fixed-aperture photometry tends to underestimate the S/N in O_{350} , which would mistakenly select low- z galaxies as the dropout candidates.

To minimize the contamination by low- z interlopers, we also limit half-light radius along the major axis of SExtractor to $0.''3$ (or ~ 1.7 kpc at $z \sim 6$), the observed upper limit for $z > 6$ galaxies at the present magnitude limit (e.g., Oesch et al. 2010; Shibuya et al. 2015; Holwerda et al. 2015; Kawamata et al. 2017).

We then follow the color-cut criteria proposed by C16 for the selection of $z \sim 10$ and $z \sim 9$ candidates, whose 95% confidence regions correspond to $7.7 < z < 9.7$ (with a peak at $z \sim 8.7$) and $z > 9.3$, respectively;

- $z \sim 10$ candidates ($J_{125}H_{160}$ -dropouts)

$$S/N_{350} < 1.5$$

$$S/N_{105} < 1.5$$

$$S/N_{160} \geq 6$$

$$J_{125} - H_{160} > 1.3$$

- $z \sim 9$ candidates ($Y_{105}JH_{140}$ -dropouts)

$$S/N_{350} < 1.5$$

$$S/N_{140} \geq 6$$

$$S/N_{160} \geq 4$$

$$Y_{105} - JH_{140} > 1.5$$

$$Y_{105} - JH_{140} > 5.33 \cdot (JH_{140} - H_{160}) + 0.7$$

$$JH_{140} - H_{160} < 0.3$$

Colors are calculated after correcting for Galactic dust extinction, where $E(B - V)$ is retrieved from the NASA/IPAC infrared archive (Schlegel et al. 1998; Schlafly & Finkbeiner 2011).⁵ We assume the canonical Milky Way dust law (Cardelli et al. 1989) to calculate the extinction in each filter.

The observed flux is scaled by $C_{160} = f_{\text{AUTO},160}/f_{\text{iso},160}$ for the following analysis, where $f_{\text{AUTO},160}$ and $f_{\text{iso},160}$ are the AUTO (i.e. total) flux and isophotal flux of SExtractor measured in H_{160} , so as to correct the flux missed in the isophotal flux. The scale factor of individual objects is applied to the other four bands to uniformly scale the fluxes.

The selected sources are shown in Figure 1. There are 15 and 19 sources selected with the color criteria for $z \sim 10$ and $z \sim 9$ candidates, respectively, up to $H_{160} \sim 27$ mag. The color near the Lyman break ($J_{125}H_{160}$ and $Y_{105}JH_{140}$) is calculated with the 1σ limiting magnitude of each image when the magnitude at the shorter wavelength has $S/N < 1$, and shown as a lower limit in Figure 1.

While our color selection mostly excludes sources with optical detection, we found in the visual inspection (Section 2.4) that some candidates show tiny blobs in O_{350} , despite satisfying $S/N_{350} < 1.5$ in the isophotal magnitude. Given its bright/extended appearance in longer wavelength filters, we consider this as sub-galactic scale/patchy star formation from dusty galaxies at lower redshifts (see Section 2.5). We therefore exclude those with $S/N_{350,\text{ap.}} > 1.5$ in addition to the criteria above, where $S/N_{350,\text{ap.}}$ is a signal-to-noise ratio measured in a small aperture (radius of 2 pixels, or $0.''16$). The aperture photometry maximizes the S/N inside objects

⁴ <http://lacosmic.readthedocs.io/en/latest/>

⁵ <http://irsa.ipac.caltech.edu/applications/DUST/>

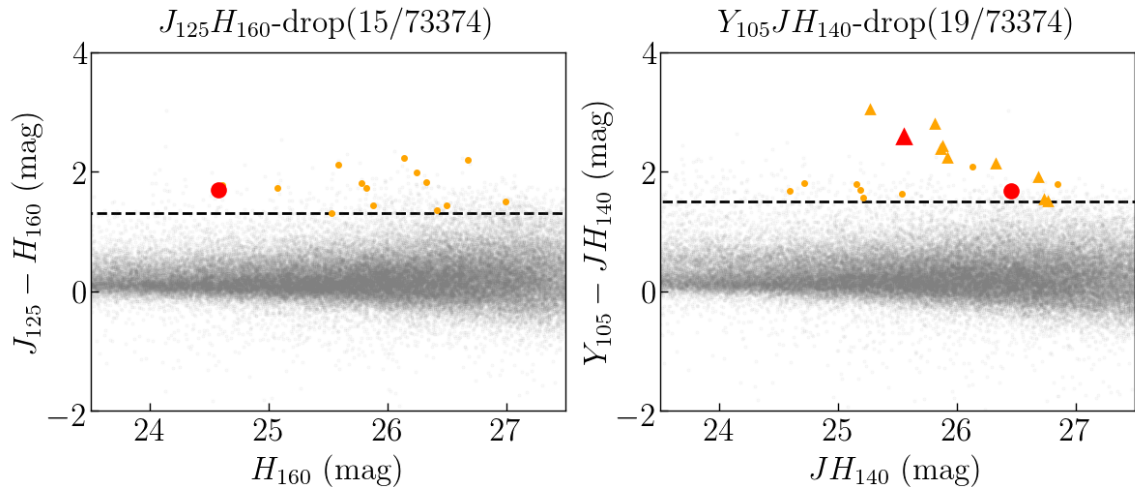


Figure 1. Color-magnitude diagram for the 79 BoRG[z9] fields. Out of 73374 detected sources (gray points), 15 and 19 objects are selected as initial $z \sim 10$ (left) and $z \sim 9$ (right) candidates, respectively (orange circles for those with measured color and triangles for those with a lower limit). The criterion for the Lyman-break color cut is shown with a dashed line. We apply visual inspection (Section 2.4), photometric redshift selection (Section 2.5), and *Spitzer* photometric selection (Section 2.6) to the initial candidates in order to select the final candidates (large red symbols).

for this case, while isophotal flux is typically measured in a larger aperture from detection images ($JH_{140}+H_{160}$ band in this study) and could lower S/Ns at shorter wavelength. This excludes one of the $z \sim 9$ candidates selected with the default criteria, while there are no such objects in $z \sim 10$ candidates. The remaining candidates are taken through the following selection process.

2.4. Visual Inspection

Four of the authors (T.M., M.T., M.S., and R.C.L.) visually checked the color-selected candidates, because we are not able to exclude artificial objects, such as PSF spikes and residual cosmic rays with only the color criteria. We exclude five objects selected as $z \sim 10$ candidates and five selected as $z \sim 9$ candidates. Those are stellar spikes, cosmic rays, or inappropriately deblended fragmentation of large galaxies.

We also check the persistence among candidates by inspecting the individual fields.⁶ We conclude that none of the remaining candidates is affected by persistence.

2.5. Photometric Redshift Selection

2.5.1. A flat prior

While the color selection is known as a standard method to efficiently select high- z candidates with minimum filter requirements, the result is binary (i.e. yes or no). In other words, the color selection by itself does not tell us how reliable those selected candidates are. To quantify the candidate selection, we use photometric redshifts as additional information. While their accuracy strongly depends on the number of filters and their depth, photometric redshifts allow us to investigate the consistency of the color selection, quantify the robustness, and eliminate unlikely candidates, if any.

We use EAZY (Brammer et al. 2008, version of 2015 April 20) to derive photometric redshifts for our candidates selected in Section 2.3. The default template set (v1.3) is used with a minor but key modification that imposes the template age to be lower than the age of the universe at the redshift derived. The choice of the template set is based on the test by Brinchmann et al. (2017), where they tested all template sets

in EAZY and found that the least biased template for high-redshift galaxies is the v1.3 template. This template is based on the original EAZY template that was developed from synthetic galaxy photometry using SAMs, but also includes several additional spectral energy distributions (SEDs) (Bruzual & Charlot 2003; Maraston 2005; Erb et al. 2010) and emission lines (Ilbert et al. 2009). We also add young star forming galaxy templates with dust attenuation up to $A_V = 4.5$ mag, because those at $z \sim 2$ resemble SEDs of high- z galaxies (Salmon et al. 2018).

While there are several choices of priors for low- z galaxies (e.g., as a function of apparent magnitude/color), we start with a flat prior (but see also below). We adopt the redshift at the peak probability distribution as the best-fit redshift (z_a).

With this setup, we found an excellent agreement for all of $z \sim 10$ candidates with the target redshift of the color selection, while this decreases to $\sim 60\%$ for $z \sim 9$ candidates. Those with inconsistent photometric redshifts show widely extended probability distributions. This is partly because the color near the Lyman break is not as strong for those galaxies as for those of other candidates with consistent redshifts. The color of the Lyman break for the strongest candidates is $\gtrsim 2$ mag, while $\sim 50\%$ of the rejected sources have a bluer color. That is, they are located near the boundary of the selection box and could have been scattered into the box due to photometric noise. We here exclude four of $z \sim 9$ candidates that have a low- z peak probability of $> 20\%$ of the high- z peak probability.

2.5.2. Building a practical prior

A flat prior is often assumed for Lyman break galaxies at high z , since it is still unclear whether applying priors from low redshift is appropriate (Benítez 2000; Salmon et al. 2017; Salvato et al. 2018). On the other hand, we know that the LF of galaxies evolves strongly from $z \sim 10$ to 0 (e.g., Behroozi et al. 2013; Bouwens et al. 2015b; Mason et al. 2015a; Kelson et al. 2016; Oesch et al. 2018). Combining the intrinsic evolution with changes in the distance modulus with redshift, we should, at a given luminosity, expect many more galaxies at lower redshift in a given survey area (Stiavelli 2009; Vulcani et al. 2017). This effect has not been taken into account yet in this study.

⁶ <https://archive.stsci.edu/prepds/persist/search.php>

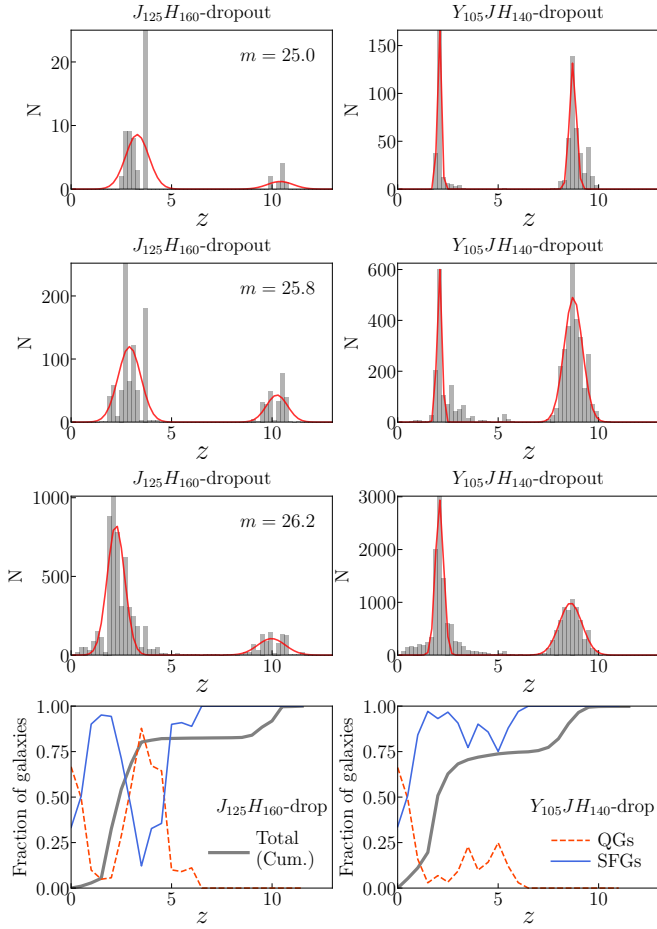


Figure 2. Examples of intrinsic redshift distributions of dropout candidates selected in the mock catalog at different magnitude bins. Each histogram is fitted with a double-peaked Gaussian (red solid lines) and used as a photometric redshift prior (Section 2.5.3). The best-fit parameters for Gaussian fitting are summarized in Table 1. The bottom panel shows the fraction of star-forming (blue solid lines) and quiescent galaxies (red dashed lines) selected as dropout candidates ($H_{160} > 24.5$ mag). The total number of mock galaxies is shown as a cumulative fraction (gray solid lines). While low- z interlopers of $z \sim 10$ candidates consist of both populations, those of $z \sim 9$ candidates are mostly star-forming galaxies.

Motivated by this fact, we design an empirical prior based on a combination of deep observations and theoretical modeling, which aims at quantifying the relative abundance of high- z sources versus low- z interlopers for color selected samples using the dropout technique. To construct such prior, we start from a mock galaxy catalog by Williams et al. (2018). While the catalog (v1.0) has been primarily aimed at planning observations with the *James Webb Space Telescope* (*JWST*), based on real deep surveys with multi-band including most *HST* broadband filters, it reproduces observed galaxy properties self-consistently, such as LF evolution up to $z \sim 8$. Therefore, it is well suited for our purposes.

The model flux in the catalog for each galaxy is perturbed to simulate observed fluxes. We assume Gaussian noise based on our limiting magnitudes. In addition to this random noise added to the model flux, we fluctuate the intrinsic flux by 0.3 dex at each redshift bin (whose width is $\delta z = 0.1$), to partially take into account the effect of cosmic variance (Somerville et al. 2004; Trenti & Stiavelli 2008), which is not reflected in the original catalog based on relatively small-volume observations. While this is a simplified

Table 1
Gaussian parameters for redshift priors

m_{160}	$A_{z,1}$	$\mu_{z,1}$	$\sigma_{z,1}$	$A_{z,2}$	$\mu_{z,2}$	$\sigma_{z,2}$	$f_{\text{int.}}^{\dagger}$
<i>J</i> ₁₂₅ <i>H</i> ₁₆₀ -dropouts							
25.00	0.87	3.29	0.57	0.13	10.43	0.58	0.83
25.25	0.66	3.13	0.60	0.34	10.53	0.12	0.86
25.50	0.57	3.13	0.62	0.43	10.51	0.12	0.82
25.75	0.74	2.90	0.56	0.26	10.24	0.52	0.76
26.00	0.77	2.51	0.61	0.23	10.11	0.62	0.77
26.25	0.89	2.23	0.43	0.11	9.97	0.69	0.86
<i>Y</i> ₁₀₅ <i>JH</i> ₁₄₀ -dropouts							
24.50	0.43	2.12	0.08	0.57	8.76	0.14	0.30
24.75	0.56	2.09	0.10	0.44	8.72	0.16	0.37
25.00	0.57	2.07	0.10	0.43	8.72	0.17	0.38
25.25	0.61	2.06	0.09	0.39	8.75	0.26	0.36
25.50	0.70	2.16	0.06	0.30	8.76	0.34	0.34
25.75	0.55	2.08	0.12	0.45	8.74	0.46	0.35
26.00	0.60	2.08	0.16	0.40	8.70	0.51	0.44
26.25	0.75	2.08	0.20	0.25	8.61	0.57	0.65
26.50	0.86	2.07	0.28	0.14	8.47	0.66	0.84
26.75	0.88	1.99	0.59	0.12	8.31	0.78	0.92

Note. — For *J*₁₂₅*H*₁₆₀-dropout candidates with $m_{160} < 25$ and > 26.25 mag, reliable Gaussian fitting parameters are not available from the small sample size. We instead adopt those from $m_{160} = 25$ and 26.25 mag for candidates, respectively. \dagger : Fraction of low- z interlopers.

approach, shifting magnitude artificially adds ~ 0.4 dex variation in galaxy number densities at $M_{UV} \lesssim -20$. We repeat this 10000 times (i.e. 10000 mock catalogs with different cosmic fluctuations, where each object has Gaussian random noise added to its flux), then select dropout candidates with our color criteria from all catalogs. The only difference is the use of F435/606/814W bands in the mock catalog, because O_{350} flux is not listed in the original catalog. We estimate the weighted mean flux from the three optical bands as

$$f_{350} = \sum_i f_i \times w_i / \sum_i w_i \quad (1)$$

where the weight is the convolution of transmission in each filter with O_{350} ,

$$w_i = T_i * T_{350}. \quad (2)$$

From the mock catalog, we estimate the fraction of low- z interlopers that are selected with our color selection, as a function of magnitude and redshift. We define low-redshift interlopers as those with intrinsic redshift at $z < 8$ but satisfy the color-color selection criteria in Section 2.3.

Figure 2 shows examples — the *intrinsic* redshift distributions of the dropout candidates at a given *observed* H_{160} magnitude. The fractions of interlopers ranges from $\sim 70\%$ ($\sim 40\%$) to $\gtrsim 85\%$ ($\sim 90\%$) for $z \sim 10$ ($z \sim 9$) candidates from $H_{160} \sim 24.8$ mag to 26.5 mag, which is consistent with the analysis of Vulcani et al. (2017).

The interloper population is dominated by $z \sim 2-3$ galaxies. The fraction of star-forming/quiescent populations in the low- z interlopers is shown in the bottom panel of Figure 2. While the low- z interlopers of $z \sim 10$ candidates consist of both populations, i.e. the star forming population at $z \sim 2$ and quiescent population at $z \sim 3.5$, those of $z \sim 9$ candidates are dominated by the star-forming population at $z \sim 3$. For *Y*₁₀₅*JH*₁₄₀ dropout candidates, the fraction of low- z interlopers increases as it approaches the magnitude ($H_{160} \sim 26.5$), be-

cause of large photometric flux errors start to affect the sample selection. On the other hand, for $J_{125}H_{160}$ dropout candidates it shows a rather flat distribution over the magnitude range. This is partly due to different selection effects for the color selection criteria—while $Y_{105}JH_{140}$ dropout candidates are mainly affected by photometric error, $J_{125}H_{160}$ dropout candidates are contaminated mainly by systematic effects due to, e.g., a smaller number of filters to characterize the Lyman break.

2.5.3. Application of the redshift prior

In general, a redshift posterior is calculated as

$$p(z|C, m) \propto p(z|m)p(C|z), \quad (3)$$

where $p(C|z)$ is a likelihood (derived by `EAZY`) given the data C . $p(z|m)$ is a prior as a function of m (e.g., magnitude; Benítez 2000). In the present study, since we first select galaxies with color criteria, an additional term is implicitly implemented in Equation 3:

$$p(C) = \begin{cases} 1, & \text{if objects satisfy the color selection} \\ 0, & \text{otherwise} \end{cases}$$

With this, redshift distributions derived in the previous section (Fig. 2) can be used as priors, $p(C)p(z|m)$, in the calculation of posterior for our preselected candidates.

To build a functional form for priors, we fit the redshift distribution with a dual-peak Gaussian model, $p(C)p(z|m) = \sum_{i=1,2} G_i(z|I_i, m)$, where $I_i = \{A_{z,i}, \mu_{z,i}, \sigma_{z,i}\}$ is the parameter set for the Gaussian fit, $G_i(z|I_i) = A_{z,i} \exp[-(z - \mu_{z,i})^2 / 2\sigma_{z,i}^2]$. The best-fit parameters (χ^2 minimization) are summarized in Table 1. Due to the small number of galaxies, Gaussian fits for $z \sim 10$ candidates in the $H_{160} \lesssim 25$ and $\gtrsim 26.3$ mag bins are not available. We instead extrapolate without changing the parameter values from the 25 mag and 26.25 mag bins to those magnitude bins, respectively.

Given the smaller error in H_{160} magnitudes (< 0.2 mag) compared to the magnitude bin of the prior, we simply multiply the fitted Gaussian function by each redshift probability distribution derived with a flat prior in the earlier part of this section. We use the redshift at the peak of the posterior distribution as the final redshift (z_{prior}). We exclude those candidates with a low- z peak probability of $> 20\%$ of the high- z peak probability, based on the typical contamination fraction at $z \sim 10$ (Pirzkal et al. 2013). Thus, the photo- z selection assures 80% reliability, or equivalently a contamination fraction $f_{\text{cont}} = 0.2$ (Section 4.2). We reject nine and five of the remaining $z \sim 10$ and $z \sim 9$ candidates, respectively.

While the mock catalog of Williams et al. (2018) reproduces the observed LFs at $z \lesssim 8$ sufficiently well, we note that galaxies at $z > 8$, especially at the bright end, are yet uncertain, and a priori assumption, such as the Schechter-form LF, may no longer be appropriate. It is also possible that samples might be somewhat affected by currently unaccounted for contamination by a class of rare intermediate-redshift galaxies with observed colors similar to those of $z \gtrsim 9$ sources. Yet, all our final candidates have a low likelihood of being interlopers (less than 20%), regardless of the application of the prior, strengthening confidence in their high- z nature. In fact, the application of the prior suppresses high-redshift probabilities for most of our cases (Table 1), and thus it offers a more conservative candidate selection. Of course, further follow-up of our candidates with deeper imaging, or spectroscopy, would represent an independent assessment of the selection.

2.6. Spitzer/IRAC photometry

For further validation of our candidates, we check the availability of public *Spitzer* data⁷ acquired from multiple *Spitzer*/IRAC 3.6 μm observations of BoRG fields (PIs S. Bernard, R. Bouwens, B. Holwerda; $m_{5\sigma} \sim 25$ -26.5 mag). While the data set does not offer complete coverage of the entire BoRG[$z9$] survey, IRAC photometry is capable of efficiently excluding low- z interlopers in the case of significant excess of flux compared to the H_{160} band such as, e.g., quiescent+dusty SEDs at $z \sim 2.5$ (Holwerda et al. 2015; Oesch et al. 2016; Salmon et al. 2018).

The $z \sim 10$ candidate has an IRAC 3.6 μm coverage. This candidate is located near a bright galaxy, where the photometry in the IRAC band is challenging with aperture photometry (Fig. 3). To extract the flux from the candidate, we use TPHOT (Merlin et al. 2016), which models the IRAC flux based on the light profile obtained from the high-resolution *HST* images. We use the $JH_{140}+H_{160}$ image as the reference model and a convolution kernel that is constructed from the PSFs in the H_{160} and IRAC 3.6 μm bands. This approach yields an extracted model magnitude of $m_{3,6} = 23.8 \pm 0.7$ for the candidate. By including this IRAC flux in the photometric redshift code, the low- z probability peak is $\sim 16\%$ of the high- z peak, and thus we retain the galaxy as the final, and the only, $z \sim 10$ candidate in this study (Fig. 3).

One of the $z \sim 9$ candidates, 0956 + 2848-98, has IRAC 3.6 μm coverage, but shows no detection ($S/N < 1$), and a 1σ lower limit is available from the rms map (> 25.5 mag; Fig. 4). The photometric redshift of the source including the IRAC upper limit remains unchanged, and thus we retain this in the sample of final $z \sim 9$ candidates.

2.7. Additional F098M photometry

One of our $z \sim 9$ candidates is by chance overlapping with previous archived observations, both from the Hubble Infrared Pure Parallel Imaging Extragalactic Survey (HIPPIES) pure-parallel program (GO 11702; PI: Yan; ~ 10 orbits) and from a previous BoRG campaign (~ 1 orbit). Combining all data, and in particular thanks to the very deep GO 11702 exposure, the object shows a significant detection in the deep F098M image, $m_{098} = 27.1 \pm 0.2$. The most likely photometric redshift for this object becomes $z \sim 2.2$, and thus we exclude it from the final candidate sample. Two other $z \sim 9$ candidates, which were reported in C16, have also been recently followed up with the same filter (1 orbit; Livermore et al. 2018). The follow-up data revised the redshift to $z \sim 1.8$ for one of the two galaxies (while confirming the high- z nature of the other), and thus this source is not included in our final sample.

This suggests that, even after the stringent selection of this study, low- z interlopers could be selected as final high- z candidates. While our final candidates show low probability peaks at low z ($\lesssim 16\%$), additional imaging around the putative Lyman break would sample the SED more accurately and further improve the quality of the high- z photometric candidates in the absence of spectroscopic confirmation. Deep *Spitzer* data would constrain the rest-frame optical wavelength range, but only if sources are well isolated (see the case for 2140 + 0241-303). Space-based deep medium-/narrowband observations, as in the BoRG Cycle 25 program (Livermore et al. 2018), are ideal before the advent of next-

⁷ <http://archive.spitzer.caltech.edu>

generation facilities such as *JWST* (see also Appendix C).

2.8. Absolute Magnitude

The UV absolute magnitude at rest-frame 1450 Å, M_{UV} , is then calculated based on the photometric redshift (i.e. the k -correction) and scaled H_{160} magnitude (Section 2.3). We assume log-normal SED with a UV slope $\beta = -2.0$ ($f_\lambda \propto \lambda^\beta$), appropriate for the high- z population (e.g., Fan et al. 2003; Bouwens et al. 2014). We checked that our choice of β from observed values (~ -1.5 to -2.0 for $M_{UV} = -23$ to -20 ; Bouwens et al. 2014) does not change our final result.

2.9. Magnification bias

Among the sample, three candidates have neighboring foreground objects in each FoV. The observed light from those high- z candidates is thus possibly affected by the gravitational potential of the foreground objects.

We calculate the magnification by foreground objects in the same manner as Mason et al. (2015b). Briefly, the photometric redshift of low- z objects is derived with EAZY. The probability distributions for both foreground and high- z candidates, and their separation, are then used to estimate the magnification. Single isothermal spheres are assumed for the mass profile of foreground deflectors. The Einstein radius of deflectors is estimated from photometry using a redshift-dependent relation of Faber & Jackson (1976). The resulting magnifications are $1.5^{+0.7}_{-0.3}$ (2140+0241-303), $1.1^{+0.1}_{-0.1}$ (0751+2917-499), and $1.7^{+0.5}_{-0.4}$ (2229-0945-394). The error in magnification is also integrated into the calculation of absolute magnitude.

3. Final candidates

Through the selection processes described in Sections 2.3 to 2.6, we have collected one $z \sim 10$ and two $z \sim 9$ candidates (Figs. 3 and 4). These candidates show extended morphology in H_{160} ($> 0.''16$; compare $r_{\text{PSF}} \sim 0.''1$ for WFC3IR). In addition, their red colors in $Y_{105} - JH_{140}$ assure that these are unlikely to be Galactic dwarf stars (Oesch et al. 2013). The photometric properties and redshifts of the final candidates are summarized in Table 2, while those initially selected with the color selection but later rejected are presented in Appendix B. Here we look at the final candidates in detail before proceeding to estimation of the number density.

3.1. Comparison to Calvi et al. (2016)

Part of our data (36 fields; $\sim 40\%$) has been studied in C16. While the initial color selections are identical in both studies, the application of our selection processes, in addition to the update in drizzle pipeline parameters and SExtractor parameters, may affect the final sample. In what follows, we compare our candidates with those presented in C16.

3.1.1. $z \sim 10$ candidates

Both C16's $z \sim 10$ candidates are rejected in the present study (as 2134-0708-645 and 2140+0241-38). These objects have consistent photometric properties between the two studies, including photometric redshift, though C16 used the BPZ photo- z code (Benítez 2000; Coe et al. 2006). However, the first object has an inconsistent photo- z after the application of our phenomenological prior (2134-0708-645 in Table 6). In fact, the probability distribution of this object had a secondary peak at $z \sim 4$ (see Figure 4 of C16; $\sim 40\%$ of the high- z peak), and the rejection after the application of our new

prior is not surprising. The second object has large apparent size ($r_{50} \sim 0.''5$) and is excluded by the size criterion.

On the other hand, we find a new candidate (2140+0241-303; Fig. 3), which was oddly not presented in C16. We find that this object was rejected because of an infinity value in its flux measurement, which came from the artificial values (NaN) in the original rms map in C16. As described in Section 2.2, we mask pixels with the artificial value when calculating their source fluxes for all images in this study. The treatment establishes this source as a viable $z \sim 10$ candidate.

This candidate is much brighter ($H_{160} \sim 24.4$ mag) than any other candidates reported at $z > 8$ so far (Coe et al. 2013; Zitrin et al. 2015; Oesch et al. 2016; Stefanon et al. 2017; Salmon et al. 2018). Even after correction for magnification (Section 2.9), this candidate has an apparent magnitude of ~ 25 mag, corresponding to $M_{UV} \sim -22.7$ mag, making it as one of the brightest objects at high z (see also Fig.3 of Salmon et al. 2018). Without additional data, we cannot reject any contribution from non-stellar components, such as AGNs.

This candidate shows a small central blob in Y_{105} , despite its non-detection with isophotal flux ($S/N = 0.9$). As for O_{350} (Section 2.3), we measure the S/N in a small aperture ($r = 0.''16$) in Y_{105} , still finding no significant detection ($S/N \sim 1.4$). Since the exposure in this field is relatively shallow (two orbits), follow-up observations at $\sim 1.1 \mu\text{m}$ would be extremely useful to elucidate this source.

Another caveat is its clustering properties. By nature, bright objects are preferentially found in dense environments and thus neighboring objects are also expected (Muñoz & Loeb 2008; Trenti & Stiavelli 2008; Ishigaki et al. 2016; Harikane et al. 2018). However, with moderate depth of imaging, clustering is not expected to play a significant role in discriminating the nature of the candidate (Ren et al. 2018). Not finding any dropout companions around this object is not unusual with our current imaging data. To further confirm any dropout clustering, deeper ($\Delta m \sim 2$ mag) follow-up observations would be required.

3.1.2. $z \sim 9$ candidates

Two of three $z \sim 9$ candidates in C16 are selected here (0956+2848-98 and 2229-0945-394) with consistent photometric properties, and successfully pass all the selection processes in the present study.

The third C16's candidate also satisfies all selection criteria in this study (0116+1425-442). However, a follow-up study with *HST* F098M imaging finds this object to be a low- z interloper at $z \sim 1.8$ (Livermore et al. 2018), as we described in Section 2.7.

4. Results

4.1. Effective Volume

We calculate the effective volume by following Oesch et al. (2012) and C16 (see also Carrasco et al. 2018, for a public code based on the same approach adopted here). Briefly, we added artificial sources in empty regions of each science frame. Those sources were modeled with realistic intrinsic distributions of UV colors and half-light radii, and they had assigned redshifts and H_{160} -magnitudes to compute the selection efficiency as a function of those parameters.

The sources were modeled with a mix of $n = 1$ and $n = 4$ Sersic (1968) profiles, and with half-light radii as found in previous studies (Oesch et al. 2010; Grazian et al. 2012; Ono et al. 2013; Holwerda et al. 2015; Kawamata et al. 2015;

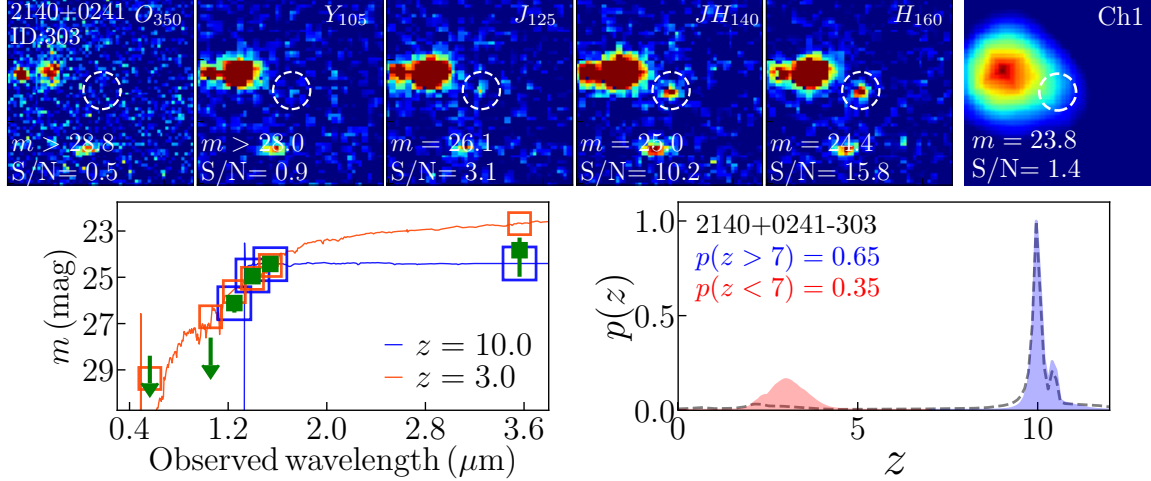


Figure 3. Final $z \sim 10$ candidate ($J_{125}H_{160}$ -dropout) that passes the color-cut criteria, visual inspection, and photometric redshift selection. *Top*: 30×30 pixel (~ 2.4 arcsec) postage stamps in five *HST* filters and IRAC ch1. The total magnitude and isophotal signal-to-noise ratio (S/N) are shown in each panel. 1σ -limiting magnitudes are shown for those without detection ($S/N < 1$). *Bottom left*: spectral energy distribution. Detection ($S/N > 1$; green squares) and 1.5σ upper limit (arrows) are shown. The best fit templates of χ^2 -minimization at high and low redshifts (blue and red solid lines, respectively) are shown, with expected fluxes at each observed band (open squares). *Bottom right*: photometric redshift probability distributions (gray dashed line for likelihood; solid line for posterior). Total probabilities at $z > 7$ and $z < 7$ are also shown.

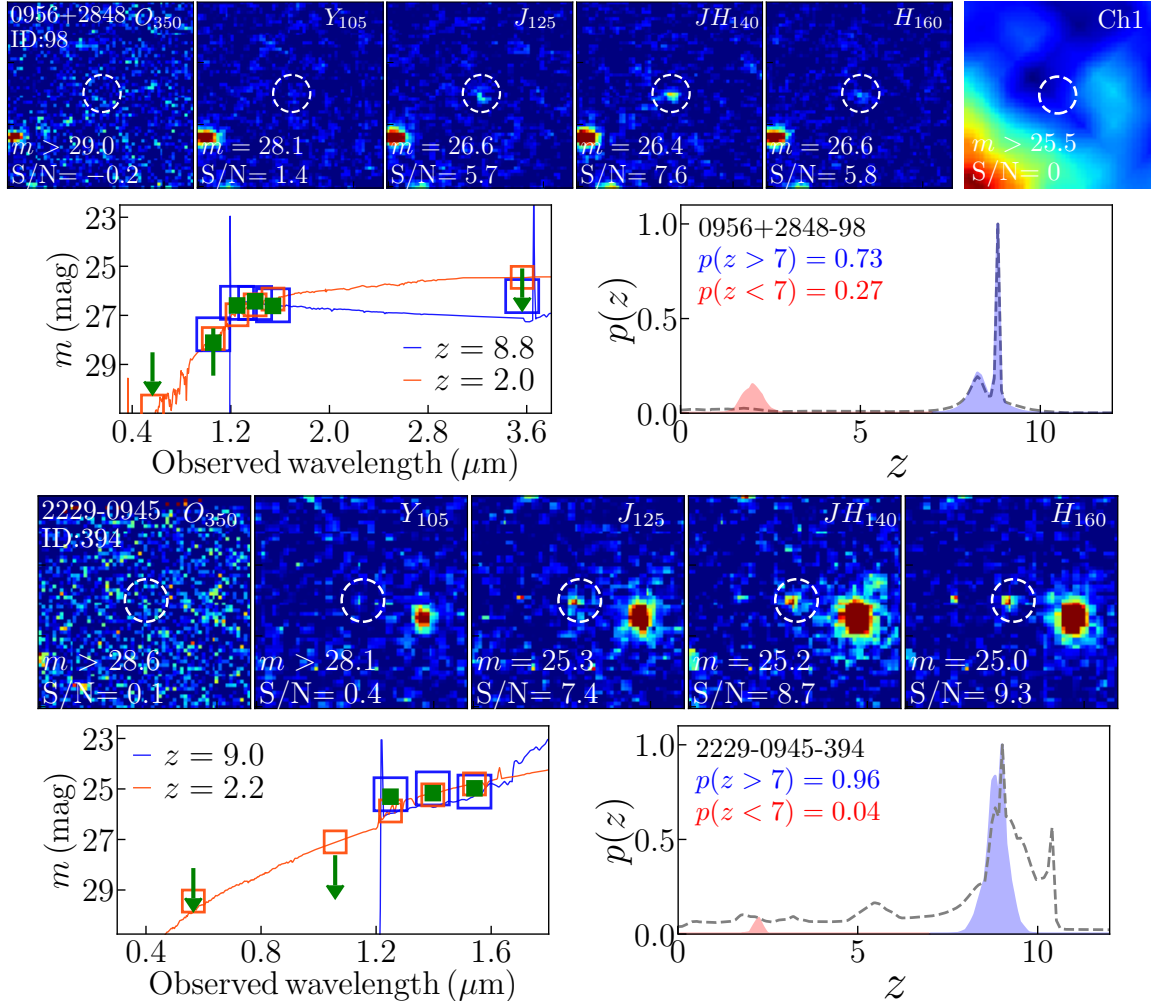


Figure 4. Same as Figure 3 but for final $z \sim 9$ candidates ($Y_{105}JH_{140}$ -dropouts).

Table 2
Coordinates and photometric properties of final $z \sim 10$ and $z \sim 9$ candidates

Object ID	α (J2000) (deg)	δ (J2000) (deg)	H_{160} (mag)	Colors		$O_{\text{ap.}}$	O_{350}	S/N				$z_{\text{phot.}}$ flat prior	M_{UV}^{\dagger} (mag)	r_{50}^{\dagger} (arcsec)	
				C_1	C_2			Y_{105}	J_{125}	JH_{140}	H_{160}				
$z \sim 10$ candidates															
2140+0241-303	324.885438	2.685170	24.4	1.7 ± 0.3	0.5 ± 0.1	0.3	0.5	0.9	3.1	10.2	15.8	10.0	10.0	$-22.6^{+0.4}_{-0.2}$	0.18
$z \sim 9$ candidates															
0956+2848-98	149.122734	28.792008	26.6	1.7 ± 0.8	-0.2 ± 0.2	-0.2	-0.2	1.4	5.7	7.6	5.8	8.8	8.8	$-20.7^{+0.1}_{-0.2}$	0.17
2229-0945-394	337.190253	-9.749134	25.0	> 2.6	0.2 ± 0.2	0.7	0.1	0.4	7.4	8.7	9.3	9.0	9.0	$-21.8^{+0.3}_{-0.3}$	0.16

Note. — C_1 : $J_{125}-H_{160}$ and $Y_{105}-JH_{140}$ colors for $z \sim 10$ and $z \sim 9$ candidates, respectively. C_2 : $JH_{140}-H_{160}$ color for $z \sim 10$ and $z \sim 9$ candidates. $O_{\text{ap.}}$: Signal-to-noise ratio in aperture photometry (radius of $0.''16$) of O_{350} band. Column 8-12: Isophotal signal-to-noise ratio of each band. Column 13: Photometric redshift derived with a flat prior. Peak redshift is presented. Column 14: Photometric redshift derived with the modeled prior. Peak redshift is presented. Column 15: UV absolute magnitude at z_{mp} assuming $f_{\lambda} \propto \lambda^{-0.2}$. Column 16: SExtractor half-light radius measured in H_{160} .

\dagger Absolute magnitude and radius are corrected for the lens magnification (Section 2.9).

Curtis-Lake et al. 2016; Bouwens et al. 2017). We assumed that there is no significant evolution at $z \gtrsim 8$ (Wilkins et al. 2016), and modeled the SED with observed UV-slope β fixed to the $z \sim 8$ value (Bouwens et al. 2014). We calculated the completeness as a function of apparent H_{160} magnitude, $C(m)$, and the source selection function as a function of magnitude and redshift, $S(z, m)$, in each sightline by detecting those artificial sources.

The effective comoving volume is then calculated as

$$V_{\text{eff}}(m) = \int_0^{\infty} S(z, m) C(m) \frac{dV}{dz} dz, \quad (4)$$

where dV/dz represents differential comoving volume at redshift z . The total volume, the sum of the effective volume over all the effective survey fields, i.e. the region that is not occupied by bright sources, ranges from $\sim 4 \times 10^4 \text{ Mpc}^3$ to $\sim 9 \times 10^5 \text{ Mpc}^3$ for our magnitude range, $-24 \lesssim M_{UV} \lesssim -20$. The effective volume used for each magnitude bin is summarized in Table 3.

4.2. Number density of high- z candidates

With the final candidates and effective volume derived in the previous sections, we estimate the stepwise number density. The density is estimated by dividing the number of candidates at a given UV absolute magnitude by the effective volume. The 1σ confidence level is estimated by assuming a Poisson distribution (Gehrels 1986). For magnitude bins with no candidates, we show 1σ upper limits derived from the Poisson distribution and effective volume.

We also take account of contamination by multiplying by $(1 - f_{\text{cont}})$, where $f_{\text{cont}} = 0.2$ is the contamination fraction defined in Section 2.5 (see also Bradley et al. 2012; Schmidt et al. 2014). With this, the uncertainty from this arbitrary contamination fraction is now limited to $\lesssim 0.1$ dex in the estimation of the number density.

Our results are summarized in Table 3 and shown in Figure 5, where we find consistency with previous studies in BoRG (C16) and other fields (Oesch et al. 2013; Bouwens et al. 2015b; Oesch et al. 2018). Our upper limits constrain the number density at values a factor of ~ 0.3 dex lower than in C16, thanks to the volume from 79 independent fields. It is noted that since three of C16's candidates are rejected as low- z interlopers in this study, one of C16's data points at $z \sim 10$ ($M_{UV} \sim -22.3$) now becomes an upper limit.

At $z \sim 9$, we find a good agreement with theoretical expectations at $M_{UV} \gtrsim -22.5$, both semi-analytical models (e.g., Mason et al. 2015a) and cosmological simulation (e.g., Trac et al. 2015; Cowley et al. 2018; Yung et al. 2018).

At the brightest magnitude bin of $z \sim 10$, however, the estimated density is $\gtrsim 1$ dex above what theoretical models expect. While our sample size is limited, and follow-up studies are necessary to differentiate those candidates from the contamination, this may highlight factors that were missed in previous models, such as evolution of the shape of LFs. The contribution of AGNs, which possibly boost the observed light of our candidates, would also be worth investigating.

5. Discussion

5.1. Impact on previous LFs at $z \sim 9$

Our magnitude range is limited to the bright end, and thus deriving robust LFs with the present data alone is challenging. Still, it is worth investigating how much our new candidates

influence LFs derived in previous studies that focused on faint objects but with limited volume, where bright objects could be easily missed. We attempt here to combine our $z \sim 9$ candidates with those in Ishigaki et al. (2018) and investigate the impact on the best-fit parameters.⁸

The $z \sim 9$ candidates in Ishigaki et al. (2018) are selected by color-color selections from all the *Hubble Frontier Fields* ($\sim 56 \text{ arcmin}^2$ in total), similar to our scheme. We take the data points of stepwise LFs in their Figure 4, which already takes into account the effect of lens magnification. While their samples include those with photometric redshifts inconsistent with the selection, we still use their values to reproduce their best-fit parameters of LF. The error, dominated by Poisson error, is recalculated in the same manner as ours.

We first fit only their points with a similar technique, Markov Chain Monte Carlo (MCMC) method, to see if our fitting method reproduces their Schechter function fit:

$$\begin{aligned} \phi(M_{UV}) = & \frac{\ln 10}{2.5} \phi^* \times 10^{0.4(\alpha+1)(M_{UV}-M_{UV}^*)} \\ & \times \exp[-10^{-0.4(M_{UV}-M_{UV}^*)}] \end{aligned} \quad (5)$$

We use the `emcee` code (Foreman-Mackey et al. 2013), assuming flat priors in the following ranges: $\alpha \in [-10 : 0]$, $M^* \in [-30 : 0]/\text{mag}$, and $\log \phi^* \in [-10 : 0]/\text{Mpc}^{-3}$. The calculation is repeated for $N_{\text{mc1}} = 10000$ times, and the first half realization is discarded to avoid the bias from initial parameter values. The best-fit values and uncertainties (16/50/84th percentiles) are calculated from the rest of the chain.

When all the parameters are set as free, the fitting results are unconstrained with large uncertainty, as also seen in Ishigaki et al. (2018), because the knee of the LF ($M_{UV} \lesssim 21 \text{ mag}$) is not sufficiently sampled by their data only. We then follow Ishigaki et al. (2018) and fix the two of the parameters ($\alpha = -1.96$ and $M_{UV}^* = -20.35$), finding consistent values for the others. This ensures that results with our fitting method are comparable.

We then add our data and fit with the Schechter function, but with a few updates in the treatment of uncertainties. We run the MCMC fitting routine introduced above for $N_{\text{mc2}} = 300$ times by fluctuating the data, as described in the following.

First, we fluctuate the observed flux within the random flux error and the systematic uncertainty from the magnification model in each iteration. While the latter uncertainty is relatively small for our candidates, some of those of Ishigaki et al. (2018) have large uncertainties in the magnification (by a factor of ~ 3) because of complicated cluster lens modeling.⁹

Second, we take account of the redshift uncertainty. In Ishigaki et al. (2018), they did not have a selection criterion with photometric redshifts, while our final sample does include a photometric redshift selection (Section 2.5). To make the two samples consistent, we fluctuate redshifts within their 1σ uncertainty range in each iteration and select those with $7.7 < z < 9.7$ (95% confidence interval for our $z \sim 9$ candidates) when calculating the number density. Absolute magnitudes are also recalculated based on fluctuated redshifts in this step.

⁸ We adopt the result of Ishigaki et al. (2018) because it consists of the largest survey volume down to $M_{UV} \sim -13 \text{ mag}$ at $z \sim 9$. It should therefore be least affected by adding our bright-end data points, which is ideal for our test here.

⁹ For the candidates of Ishigaki et al. (2018), we use uncertainties in photometric redshift and magnification listed in Kawamata et al. (2018).

Finally, we refine the UV magnitude grid when calculating the number density, because different grids change the stepwise number density and can affect the fitting parameters (Schmidt et al. 2014). We set the magnitude grid as $M_{UV} \in [-24 + \text{rand}(-0.5, 0.5) : -13 + \text{rand}(-0.5, 0.5)]$ with a magnitude bin size $\Delta M_{UV} = \text{rand}(0.3, 1.5)$ in each iteration, where $\text{rand}(a, b)$ is a random float value taken from the range between a and b . The effective volume is interpolated to the refined magnitude grid. Skipping the third process would underestimate the uncertainty down to $\sim 30\%$, depending on the size of the magnitude bin.

The result from combining our new observations with the literature data is shown in Fig. 6, where we find that all three parameters are constrained within physically meaningful ranges (Table 4). We present the 50/16/84th percentiles taken from the synthesized MCMC chain ($N_{\text{mc1}} \times N_{\text{mc2}}$) as the best-fit parameters. Compared to the fixed values of Ishigaki et al. (2018) ($\alpha = -1.96$ and $M_{UV}^* = -20.35$), our value for α is smaller (-2.1), and M_{UV}^* is ~ 0.6 mag smaller (-21.0), which can be understood from the fact that our data constrain the bright end at a lower number density than previously possibly.

With the best-fit Schechter parameters, we estimate the cosmic UV luminosity density,

$$\rho_{UV} = \int_{-\infty}^{M_{\text{lim}}} dM_{UV} L(M_{UV}) \phi(M_{UV}) \quad (6)$$

where $L(M_{UV})$ is the UV luminosity at a given UV absolute magnitude. As summarized in Table 4, we find $\log \rho_{UV} \sim 25.3 \text{ ergs}^{-1} \text{ Hz}^{-1} \text{ Mpc}^{-3}$ (25.6) with $M_{\text{lim}} = -17$ (-15), or $\log \psi_* \sim -2.6 M_{\odot} \text{ yr}^{-1} \text{ Mpc}^{-3}$ (-2.4) when the conversion in Madau & Dickinson (2014) is applied.

The derived value is consistent with that derived in Ishigaki et al. (2018, $\log \psi_* \sim -2.7 M_{\odot} \text{ yr}^{-1}$ with $\alpha = -1.96$ and $M_{UV}^* = -20.35$), or slightly larger than that in Oesch et al. (2013, $\log \psi_* \sim -2.9$ with $\alpha = -1.73$ and $\log \phi^* = -2.94$), but in excellent agreement with McLeod et al. (2016) and theoretical models (e.g., Tacchella et al. 2013; Mason et al. 2015b, see also Figure 5 of Oesch et al. 2018). The luminosity density derived here lies between those claimed at lower redshifts (e.g., $z \sim 8$ in Bouwens et al. 2015b) and higher redshift ($z \sim 10$ in Oesch et al. 2018).

Our updated value of the UV luminosity density does not qualitatively change the conclusion in Ishigaki et al. (2018), where they found a linear relation in z - $\log \rho_{UV}$ up to $z \sim 9$ (see also Oesch et al. 2013; Bouwens et al. 2016; McLeod et al. 2016), which may then turn into an accelerated decrease at yet higher redshift (Oesch et al. 2018).

We also fit the number density with a double power law, motivated by recent studies at lower redshift (e.g., Ono et al. 2018):

$$\phi(M_{UV}) = \frac{\ln 10}{2.5} \phi^* \times [10^{0.4(\alpha+1)(M_{UV}-M_{UV}^*)} + 10^{0.4(\beta+1)(M_{UV}-M_{UV}^*)}]^{-1}$$

We set the same prior range as above for α , M_{UV}^* , and ϕ^* , and set $\beta \in [-10 : \alpha]$. The fit shows unconstrained β and large uncertainties for the other parameters when all the parameters are free. When the characteristic magnitude is fixed ($M^* = -20.35$), the other parameters return some constrained values, but still with relatively large uncertainties ($\log \phi^* = -3.48_{-0.11}^{+0.11}$, $\alpha = -1.92_{-0.17}^{+0.17}$, and $\beta = -5.80_{-1.89}^{+2.00}$).

Table 3
Number density of dropout candidates

M_{UV} (mag)	$\log \phi$ (1/Mpc ³ /mag)	Number	V_{eff} (10 ⁴ Mpc ³)
$z \sim 10$			
-23.0	$-6.1_{-0.8}^{+0.5}$	1	95.68
-22.0	< -5.9	0	76.08
-21.0	< -4.6	0	3.80
$z \sim 9$			
-23.0	< -5.9	0	73.39
-22.0	$-5.9_{-0.8}^{+0.5}$	1	63.87
-21.0	$-5.4_{-0.8}^{+0.5}$	1	19.94

Note. — Errors of number densities are dominated by Poisson uncertainty.

Thus, we conclude that we are still unable to rule out this functional form, and that additional large-area surveys would be highly beneficial.

6. Summary

In this paper, we presented the full data set of BoRG[z9], which collected five-band imaging with *HST*/WFC3IR and UVIS from 79 independent sightlines ($\sim 370 \text{ arcmin}^2$), and we analyzed the data to investigate the number density of bright galaxies at $z \sim 10$ and 9. Our findings are summarized as follows.

- With the standard color selection, we first found 15 and 19 candidates at $z \sim 10$ and 9, respectively. Through the more strict selection process with photometric redshift and *Spitzer* photometry, we then identified respectively one and two sources as the final candidates (Figs. 3 and 4 and Table 2).
- The $z \sim 10$ candidate is one of the brightest galaxy candidates at $z \gtrsim 8$, an ideal target for follow-up observations.
- We combined our data and previous faint candidates, and constrained the Schechter LF at $z \sim 9$ without fixing any parameters for the first time.
- From the best-fit LF parameters, we derived the UV luminosity density, $\log \rho_{UV} \sim 25.3 \text{ ergs}^{-1} \text{ Hz}^{-1} \text{ Mpc}^{-3}$ (when integrated at $M_{UV} < -17$), which is consistent with an unaccelerated decreasing of the luminosity density from lower redshift.

Throughout the present study, it became clear that the selection of high- z candidates still suffers from low- z interlopers, especially with a standard color selection method (see also Vulcani et al. 2017). Thanks to our survey design, these candidates are bright and ideal for follow-up photometric and spectroscopic observations that would require only a small fraction of the time devoted to the blind initial search. Future facilities with larger fields of view, such as WFIRST (Spergel et al. 2015), will increase the number of candidates at a similar redshift range and luminosity. Its grism spectroscopic observations, or observations at longer wavelength by *JWST* (e.g.,

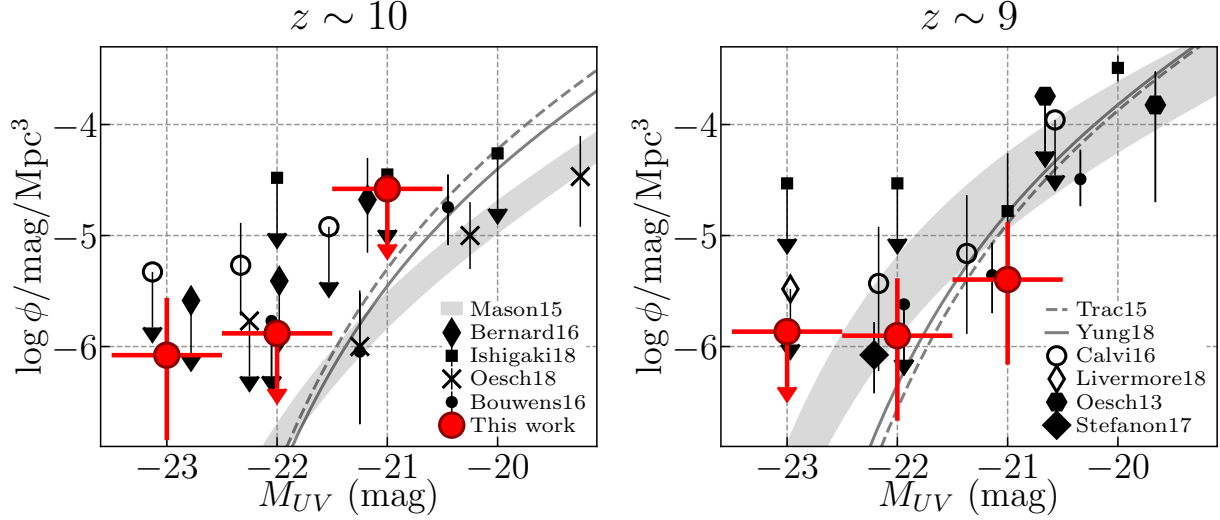


Figure 5. Number density of $z \sim 10$ (left) and $z \sim 9$ (right) candidates derived in this study. The bin size in magnitude ($\Delta M = 0.5$) is taken so that it becomes larger than the typical errors from photometric redshift and magnitude. Previous results from the partial BoRG[z9] data are shown with open symbols (Calvi et al. 2016, circles; Livermore et al. 2018, diamonds). Other results from previous observations in this magnitude range are also shown with filled symbols (Oesch et al. 2013, hexagons; Bernard et al. 2016, diamonds; Stefanon et al. 2017, large diamond; Ishigaki et al. 2018, squares; Bouwens et al. 2015b, dots; Oesch et al. 2018, crosses). Theoretical expectations of luminosity functions at $z \sim 10$ and 9 from Mason et al. (2015a, gray shaded regions), Trac et al. (2015, dash lines), and Yung et al. (2018, solid lines) are shown.

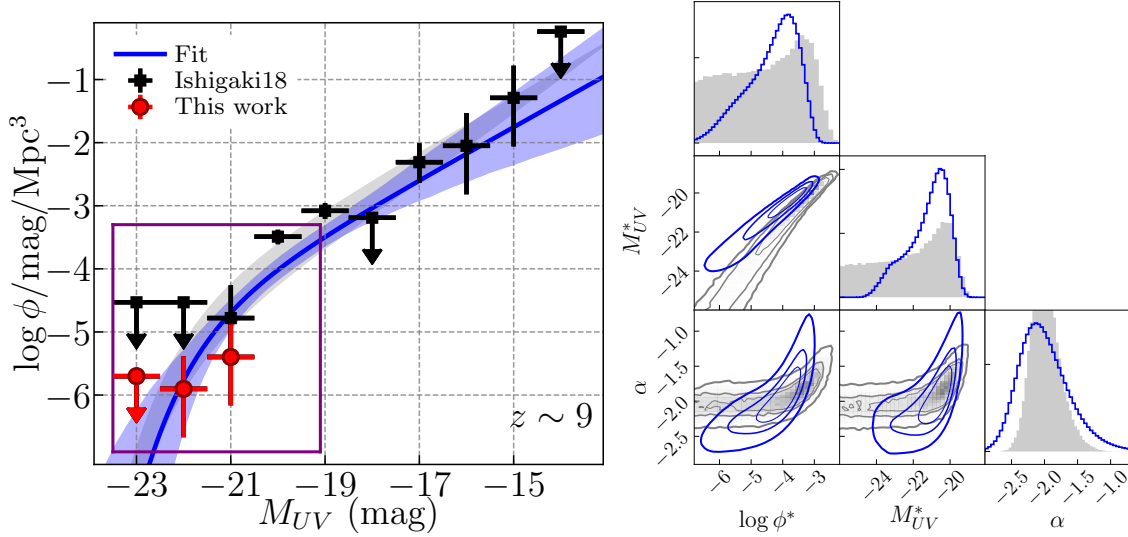


Figure 6. Left: LF fit with the Schechter function form to the combined data from this study (red circles) and Ishigaki et al. (2018, black squares). The fit with the best-fit parameters is shown with blue solid line, with its 16/84th percentiles from all the realizations (blue filled region). The theoretical LF by Mason et al. (2015a) is shown for comparison (gray shaded region). The zoomed region shown in Figure 5 is framed with purple lines. Right: Covariance matrices of the LF parameters. Fitting only with previous data from Ishigaki et al. (2018) shows unconstrained results in parameter spaces (filled gray histograms and contours; 39/68/95%), whereas inclusion of our data shows constraints for all parameters (blue contours and histograms).

Table 4
Fitting Parameters for Schechter Luminosity Function and Cosmic Star Formation Rate Density at $z \sim 9$

$\log \phi^*$ ($\text{Mpc}^{-3} \text{mag}^{-1}$)	M_{UV}^* (mag)	α	$\log \rho_{UV}$ ($\text{erg s}^{-1} \text{Hz}^{-1} \text{Mpc}^{-3}$)		$\log \psi_*$ ($M_{\odot} \text{yr}^{-1} \text{Mpc}^{-3}$)	
			($M_{UV} < -17$)	($M_{UV} < -15$)	($M_{UV} < -17$)	($M_{UV} < -15$)
$-4.24^{+0.56}_{-0.93} \quad +0.44_{-0.38}$	$-21.01^{+0.69}_{-1.35} \quad +0.58_{-0.50}$	$-2.06^{+0.31}_{-0.29} \quad +0.27_{-0.15}$	$25.33^{+0.01}_{-0.12} \quad +0.09_{-0.09}$	$25.55^{+0.10}_{-0.24} \quad +0.15_{-0.15}$	$-2.61^{+0.01}_{-0.12} \quad +0.09_{-0.09}$	$-2.39^{+0.10}_{-0.24} \quad +0.15_{-0.15}$

Note. — 50th and 16/84th percentiles are taken from the MCMC realization as the best-fit values and their uncertainties. Associated errors are random photometric errors and systematic errors from the binning size in the UV absolute magnitude. We use $\kappa_{UV} = 1.15 \times 10^{-28} M_{\odot} \text{yr}^{-1} \text{erg s}^{-1} \text{Hz}^{-1}$ (Madau & Dickinson 2014) to convert from the UV luminosity density (ρ_{UV}) to the star formation rate density (ψ_*).

Kalirai 2018), will be necessary to improve the sample quality beyond that possible with a dropout selection. In addition, such follow-up would also determine the physical properties of the objects such as stellar masses, ages, and possibly chemical composition. Given the limited lifetime of *JWST*, a BoRG-like pure-parallel observing strategy will be an efficient way of searching for the first bright galaxies at $z > 8$ both with *HST* and with *JWST*.

We thank the anonymous referee for providing constructive comments. We thank Masafumi Ishigaki for providing the data points of luminosity function in Ishigaki et al. (2018). T.M. thank Yuichi Harikane for fruitful discussion. Based on observations made with the NASA/ESA Hubble Space Telescope, which is operated by the Association of Universities for Research in Astronomy, Inc., under NASA contract NAS 5-26555. These observations are associated with programs 14701 and 13767. This research was conducted by the Australian Research Council Centre of Excellence for All Sky Astrophysics in 3 Dimensions (ASTRO 3D), through project number CE170100013. C.M. acknowledges support provided by NASA through the NASA Hubble Fellowship grant HST-HF2-51413.001-A awarded by the Space Telescope Science Institute, which is operated by the Association of Universities for Research in Astronomy, Inc., for NASA, under contract NAS5-26555.

APPENDIX

A. SURVEY FIELDS AND LIMITING MAGNITUDES

We list here exposure times and limiting magnitudes of all survey fields in the BoRG Cycle 22 observation. The 5σ limiting magnitudes are calculated from rms maps. We measure the median rms value with an $0.''32$ radius aperture in empty sky regions. Ten out of 89 original fields are discarded, either because the fields are excessively dominated by stars or the acquisition of a guide star failed. Exposure times and limiting magnitudes for all fields are summarized in Table 5.

B. REJECTED CANDIDATES

We summarize here objects that are selected in the color-color selection (Section 2.3) but rejected in the later selection processes. Out of 15 (19) objects selected with the color selection as $z \sim 10$ ($z \sim 9$) candidates, 0 (1) are rejected by the small aperture photometry in O_{350} (Section 2.3), 5 (5) by the visual inspection (Section 2.4), 0 (4) by photometric redshifts without priors (Section 2.5.1), 9 (5) by photometric redshifts with priors (Section 2.5.2), and 0 (2) with additional F098M photometry (Section 2.7). The rejected objects are summarized in Table 6.

C. IMPORTANCE OF SUPPLEMENTAL F098M PHOTOMETRY

Two among the final $z \sim 9$ candidates were rejected after adding supplemental F098M photometry (one in this study and one in Livermore et al. 2018). These candidates would otherwise have been included in the final sample, satisfying all the criteria in this study (i.e. $< 20\%$ of contamination rate). In particular, without F098M data, the redshift probability distribution for the former source included a $> 98\%$ likelihood at $z > 8$. With the F098M photometry ($m_{098} = 27.1 \pm 0.2$), the redshift probability changed dramatically, preferring a low- z result at $z \sim 2.2$ (Fig. 7).

With F098M, the SED (Fig. 7) is now fitted with a passive galaxy template, whose best-fit parameters are $\log t/\text{yr} = 8.6_{-0.6}^{+0.4}$, $A_V/\text{mag} = 0.8_{-0.8}^{+1.9}$, and $\log M_*/M_\odot = 9.7_{-0.3}^{+0.6}$, revealing this as an intermediate-mass, moderately dusty, quiescent galaxy. The SED parameters are derived from FAST (Kriek et al. 2009), assuming the dust law of Calzetti et al. (2000) and the initial mass function of Salpeter (1955). The best-fit template indicates the magnitude in Y_{105} to be ~ 27 mag.

Our results and the recent work by Livermore et al. (2018) jointly highlight the benefit from additional follow-up data with medium-band filters around the expected Lyman break in order to build reliable photometric samples. This approach is more efficient than just application of a yet stricter selection criterion (which risks decreasing significantly the selection completeness), and would require only a modest amount of additional observing time because $z > 8$ candidates are rare.

Table 5
BoRG fields coordinates, exposure times, and 5σ limiting magnitudes

Field ID	α (J2000) (deg)	δ (J2000) (deg)	No. of orbits	E(B-V)	F350LP		F105W		F125W		F140W		F160W		A_c (\square)
					t_{exp}	m_{lim}									
0058-7201*	1.458e+01	-7.201e+01	2	0.322	—	—	—	—	—	—	—	—	—	—	—
0111-7248*	1.767e+01	-7.280e+01	4	0.087	—	—	—	—	—	—	—	—	—	—	—
0116+1425	1.906e+01	1.441e+01	3	0.041	2408	26.41	1758	26.41	2058	26.54	2208	26.43	2095	27.04	4.61
0119-3411	1.968e+01	-3.418e+01	3	0.027	1758	26.05	1305	26.11	1505	25.87	1605	26.08	1306	26.96	4.62
0132+3035*	2.311e+01	3.059e+01	3	0.049	—	—	—	—	—	—	—	—	—	—	—
0132-7326	2.305e+01	-7.344e+01	2	0.073	1255	26.27	1455	26.68	1705	26.46	1805	26.30	1695	27.10	4.64
0133+3043*	2.337e+01	3.072e+01	3	0.041	—	—	—	—	—	—	—	—	—	—	—
0134+3034*	2.348e+01	3.057e+01	3	0.043	—	—	—	—	—	—	—	—	—	—	—
0134+3041*	2.343e+01	3.068e+01	2	0.041	—	—	—	—	—	—	—	—	—	—	—
0235-0357	3.880e+01	-3.944e+00	16	0.023	11246	26.97	8235	27.23	9446	27.06	9846	27.14	8286	27.66	6.35
0314-6712	4.843e+01	-6.720e+01	8	0.038	7223	27.13	5129	27.23	6123	27.28	6223	27.40	4737	27.44	5.07
0337-0507	5.437e+01	-5.115e+00	3	0.044	2408	26.45	1708	26.61	2058	26.41	2108	26.38	1967	27.07	4.76
0554-6005	8.839e+01	-6.009e+01	4	0.057	2811	26.74	2058	26.97	2411	26.85	2511	26.44	2252	27.21	4.62
0751+2917	1.177e+02	2.928e+01	4	0.043	2811	26.50	2008	26.68	2411	26.56	2461	26.53	2210	26.96	4.62
0807+3606	1.219e+02	3.611e+01	4	0.049	3111	26.45	2308	26.67	2611	26.63	2711	26.23	2693	27.05	4.64
0834+5238	1.285e+02	5.264e+01	3	0.035	1858	26.45	1355	26.64	1605	26.59	1705	26.69	1649	26.82	4.64
0851+4240	1.327e+02	4.266e+01	3	0.025	2458	26.27	1808	26.38	2108	26.29	2208	26.27	2180	26.90	4.61
0853+0310	1.332e+02	3.159e+00	3	0.050	1708	26.37	1255	26.60	1505	26.49	1555	26.61	1392	26.98	4.61
0925+1360	1.413e+02	1.400e+01	3	0.032	1858	26.22	1305	26.42	1505	26.41	1705	26.50	1510	26.90	4.62
0925+3439	1.413e+02	3.465e+01	3	0.020	2458	26.47	1758	26.52	2058	26.44	2158	26.54	2039	27.11	4.64
0948+5757	1.470e+02	5.795e+01	3	0.015	2608	26.50	1908	26.70	2208	26.34	2308	26.50	2250	26.82	4.61
0949+5759	1.473e+02	5.799e+01	4	0.014	3511	26.58	2561	26.84	2861	26.70	3111	26.78	2336	27.17	4.64
0952+5150	1.480e+02	5.183e+01	3	0.007	1758	26.23	1958	26.49	2308	26.45	2358	26.52	1845	26.69	4.62
0953+5150	1.483e+02	5.184e+01	4	0.009	2661	26.47	1958	26.67	2308	26.64	2358	26.68	1809	27.08	4.64
0953+5153	1.483e+02	5.189e+01	8	0.009	5373	26.92	3917	27.14	4617	27.10	4717	27.16	3608	27.63	4.95
0953+5157	1.483e+02	5.195e+01	4	0.010	2661	26.59	1958	26.90	2308	26.80	2358	27.00	1809	27.22	4.61
0955+4528	1.488e+02	4.547e+01	3	0.011	1858	26.27	1355	26.45	1605	26.30	1705	26.26	1504	26.95	4.64
0956+2848	1.491e+02	2.880e+01	6	0.018	4417	26.74	3214	26.85	3767	26.70	3864	26.69	2940	27.20	4.76
1015+5945	1.537e+02	5.975e+01	6	0.010	4717	26.74	3467	26.87	4017	26.60	4214	25.67	3084	26.96	4.69
1017-2052	1.544e+02	-2.087e+01	3	0.044	1058	25.96	705	26.13	855	26.07	855	26.03	900	26.77	4.64
1018+0544	1.545e+02	5.735e+00	3	0.020	2408	26.51	1758	26.70	2008	26.54	2108	26.56	2000	27.09	4.64
1048+1518	1.620e+02	1.530e+01	3	0.028	2308	26.10	1658	26.16	1958	26.11	2058	26.24	1980	26.78	4.61
1103+2913	1.657e+02	2.922e+01	4	0.029	3211	26.74	2311	26.81	2811	26.73	2911	26.77	2575	27.34	4.64
1104+2813	1.660e+02	2.821e+01	4	0.033	2861	26.41	2058	26.50	2461	26.46	2508	26.50	2275	26.98	4.63
1106+2925	1.665e+02	2.941e+01	3	0.030	2308	26.33	1605	26.43	1908	26.39	2008	26.43	1823	26.96	4.66
1106+3508	1.665e+02	3.514e+01	4	0.018	3111	26.61	2208	26.79	2661	26.80	2761	26.61	2480	27.18	4.64
1115+2548	1.687e+02	2.580e+01	4	0.017	2761	26.59	2008	26.81	2411	26.74	2461	26.80	2151	27.21	4.62
1127+2653 [†]	1.718e+02	2.688e+01	2	0.018	—	—	—	—	—	—	—	—	—	—	—
1136+0747	1.739e+02	7.786e+00	3	0.036	2408	26.43	1708	26.48	2058	26.57	2108	26.57	2113	27.06	4.64
1142+2640	1.755e+02	2.667e+01	7	0.019	4370	26.71	3214	26.89	3717	26.87	3817	26.88	3166	27.21	4.75
1142+2647	1.755e+02	2.678e+01	3	0.022	2158	26.37	1658	26.52	1908	26.33	1958	26.52	1486	26.90	4.64
1142+3020	1.756e+02	3.034e+01	3	0.021	2408	26.52	1758	26.79	2108	26.71	2158	26.78	2130	27.20	4.61
1143+3019	1.756e+02	3.032e+01	3	0.020	1808	26.35	1305	26.55	1505	26.36	1605	26.52	1266	26.88	4.63
1149+2202	1.772e+02	2.203e+01	3	0.025	1758	26.19	1305	26.28	1555	26.30	1605	26.23	1480	26.74	4.64
1152+3402	1.779e+02	3.403e+01	2	0.020	1605	26.38	1155	26.51	1405	26.44	1455	26.51	1154	26.91	4.64
1152+5433	1.779e+02	5.455e+01	4	0.010	2811	26.43	2008	26.72	1758	26.52	2461	25.82	2185	27.04	4.62
1152+5434	1.779e+02	5.456e+01	7	0.010	5070	26.64	3617	26.84	4320	26.82	4370	26.60	3947	27.33	5.81
1154+4639	1.784e+02	4.665e+01	6	0.032	3717	26.81	2711	27.03	3211	26.91	3411	27.09	2583	27.46	4.71
1160+0015	1.800e+02	2.522e-01	2	0.032	1805	26.51	1255	26.54	1505	26.44	1605	26.62	1473	26.88	4.64
1209+4543	1.824e+02	4.572e+01	7	0.014	4420	26.94	3164	27.14	3717	27.12	3917	26.75	3500	27.48	4.62
1218+3008	1.846e+02	3.013e+01	6	0.021	4067	26.73	2964	26.85	3417	26.80	3564	26.68	2764	27.20	4.65
1229+0751*	1.874e+02	7.857e+00	8	0.024	—	—	—	—	—	—	—	—	—	—	—
1313+1804*	1.982e+02	1.807e+01	4	0.020	—	—	—	—	—	—	—	—	—	—	—
1334+3131	2.034e+02	3.152e+01	3	0.012	2408	26.52	1808	26.75	2108	26.68	2108	26.55	2133	27.15	4.64
1410+2623	2.124e+02	2.638e+01	4	0.017	2811	26.63	2008	26.85	2411	26.85	2461	26.73	2210	27.21	4.62
1413+0918	2.132e+02	9.299e+00	4	0.026	3061	26.65	2211	26.68	2561	26.71	2661	26.70	2358	27.12	4.61
1421+4725	2.153e+02	4.741e+01	2	0.013	1205	26.21	1305	26.55	1605	26.38	1705	26.07	1480	26.93	4.61
1431+0259	2.179e+02	2.989e+00	4	0.029	3011	26.48	2208	26.59	2561	26.52	2661	26.47	2551	27.08	4.61
1437-0150	2.194e+02	-1.826e+00	5	0.044	3364	26.57	2461	26.66	2914	26.63	3011	26.66	2541	27.15	4.63
1438-0142	2.195e+02	-1.700e+00	7	0.043	4420	26.82	3164	26.96	3767	26.87	3917	27.03	3393	27.43	4.65
1442-0212	2.205e+02	-2.195e+00	2	0.053	1605	26.35	1155	26.46	1355	26.40	1405	26.46	1252	26.88	4.64
1503+3645	2.258e+02	3.674e+01	3	0.015	2208	26.66	1605	26.80	1908	26.69	2008	26.81	1443	27.25	4.64
1519-0746	2.298e+02	-7.767e+00	4	0.100	2511	26.34	1858	26.64	2208	26.49	2361	26.51	2244	26.91	4.63
1520-2501	2.301e+02	-2.502e+01	2	0.165	1505	26.23	1005	26.28	1255	26.29	1355	26.42	1872	27.01	4.62
1524+0956	2.310e+02	9.939e+00	5	0.042	3364	26.74	2461	26.85	2914	26.88	3011	26.85	2520	27.31	4.64
1525+0955	2.312e+02	9.921e+00	3	0.039	1608	26.14	1155	26.40	1355	26.40	1455	26.53	1230	26.87	4.61
1525+0960	2.312e+02	1.000e+01	4	0.038	2861	26.68	2008	26.87	2361	26.74	2461	26.92	2154	27.22	4.64
1536+1410	2.341e+02	1.417e+01	3	0.047	2408	26.62	1758	26.62	2108	26.74	2158	26.69	1950	27.19	4.63
1558+0812	2.396e+02	8.196e+00	3	0.039	2308	26.60	1255	26.64	955	26.27	1505	26.58	1457	27.10	4.64

Table 5
Continued.

Field ID	α (J2000) (deg)	δ (J2000) (deg)	No. of orbits	E(B-V)	F350LP		F105W		F125W		F140W		F160W		A_e (\square')
					t_{exp}	m_{lim}									
1607+1332	2.417e+02	1.354e+01	3	0.036	2408	26.60	1758	26.76	2108	26.77	2158	26.76	1975	27.13	4.64
1614+4856	2.435e+02	4.894e+01	4	0.014	3211	26.71	2308	26.97	2661	26.76	2711	26.75	2222	26.94	4.63
1619+2541	2.448e+02	2.568e+01	3	0.048	2408	26.63	1758	26.77	2108	26.72	2158	26.72	1997	27.31	4.63
1632+3736	2.479e+02	3.761e+01	12	0.010	8435	27.16	6026	27.40	7235	27.24	7385	27.34	6480	27.82	5.28
1659+3732	2.548e+02	3.753e+01	3	0.017	2508	26.60	1808	26.76	2108	26.85	2158	26.71	2179	27.38	4.62
1708+4237	2.571e+02	4.262e+01	3	0.024	2708	26.84	2108	26.90	2408	26.88	2408	26.86	2055	27.38	4.64
1715+0455	2.588e+02	4.915e+00	4	0.119	2461	26.47	1908	26.70	2261	26.66	2411	26.66	933	26.66	4.63
1715+0502	2.588e+02	5.035e+00	5	0.132	3064	26.63	2261	26.82	2661	26.71	2911	26.85	3262	27.41	4.64
1738+1839	2.644e+02	1.865e+01	2	0.061	1605	26.40	1155	26.51	1355	26.52	1505	26.32	1541	27.07	4.64
1920+4531	2.901e+02	-4.552e+01	4	0.086	2911	26.51	2058	26.74	2511	26.35	2661	26.48	2660	26.98	4.62
2008-6610	3.020e+02	-6.617e+01	2	0.071	1805	26.44	1305	26.63	1505	26.49	1605	26.07	1855	27.08	4.64
2057-1423	3.143e+02	-1.438e+01	3	0.051	1908	26.32	1505	26.53	1705	26.45	1705	26.44	1710	27.10	4.64
2134-0708	3.235e+02	-7.126e+00	6	0.033	4167	26.28	2964	26.54	3514	26.35	3714	26.27	3605	26.92	4.70
2140+0241	3.249e+02	2.690e+00	2	0.088	1605	26.37	1155	26.45	1355	26.31	1405	26.30	1872	27.09	4.61
2141-2310*	3.252e+02	-2.317e+01	3	0.049	—	—	—	—	—	—	—	—	—	—	—
2228-0955	3.371e+02	-9.920e+00	3	0.052	2408	26.38	1708	26.52	2058	26.47	2108	26.50	2093	26.97	4.64
2229-0945	3.372e+02	-9.752e+00	3	0.050	1758	26.26	1255	26.39	1505	26.40	1605	26.32	1479	26.83	4.63
2253-1411	3.434e+02	-1.419e+01	4	0.044	2761	26.57	2008	26.70	2361	26.65	2461	26.75	2174	27.09	4.61
2312-1423	3.479e+02	-1.439e+01	3	0.035	2408	26.55	1758	26.57	2108	26.72	2158	26.57	1970	27.09	4.64
2323+0059	3.507e+02	-9.841e-01	3	0.044	2408	26.37	1708	26.42	2008	26.34	2158	26.40	2095	26.94	4.63

Note. — NOTE: Column 1: Field name derived from the coordinates. Columns 2-3: α and δ coordinates (in degrees) as from the F140W exposure. Column 4: total number of *HST* orbits allocated. Column 5: Galactic extinction E(B-V) from Schlafly & Finkbeiner (2011). Columns 6-15: exposure time (in seconds) and 5σ limiting magnitude (in AB magnitudes) within a $r = 0''.32$ aperture in each band. Column 16: effective area (in arcmin^2).

* Field excessively dominated by stars.

† Guide star acquisition failure.

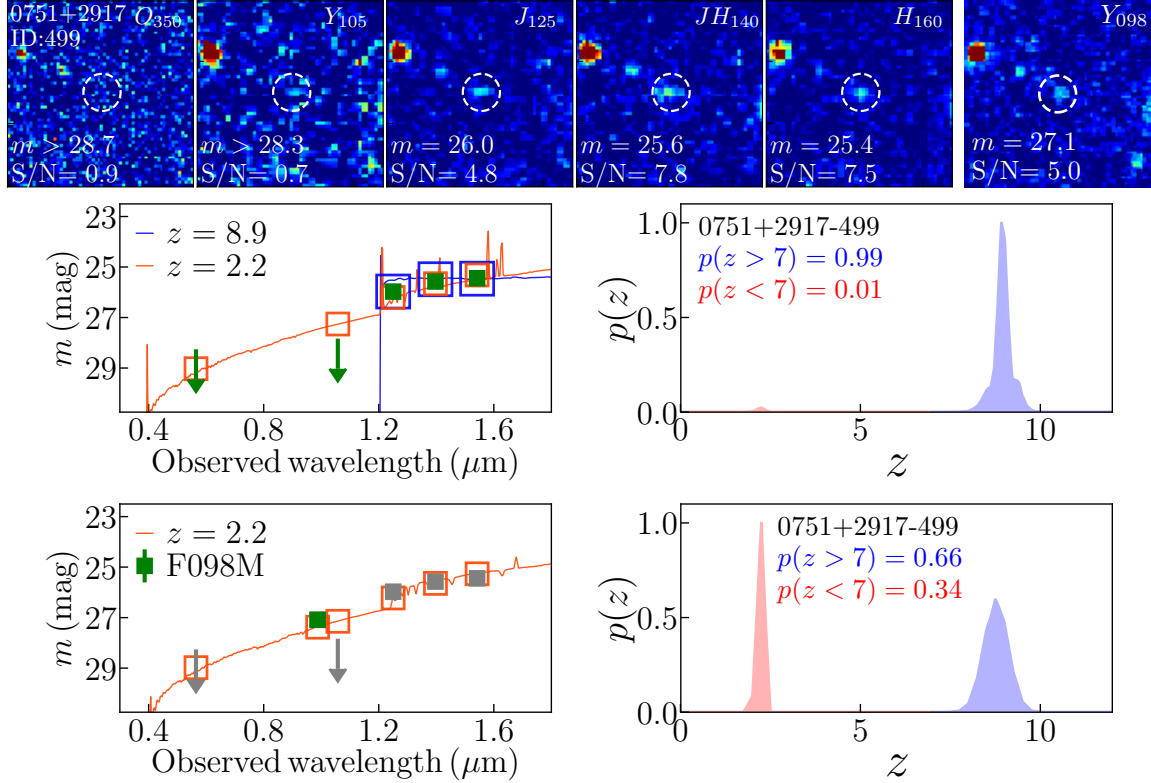


Figure 7. Same as Fig. 3 but for 0751+2917-499 with F098M detection (top right), despite the absence of clear detection in F105W. The color stretch is changed for Y₁₀₅ from other filters to stress its noise level. The central blob is hardly distinguishable from the surrounding noise either by eyes or SExtractor ($S/N = 0.7$). The non-detection in Y₁₀₅ is attributed to its shallow exposure ($t = 2008$ sec), while F098M has a much deep exposure from multiple observing programs ($t = 18642$ sec). Addition of F098M photometry dramatically changes the photometric probability distribution (from middle to bottom panels), revealing the importance of medium band photometry near Lyman breaks.

Table 6
Coordinates and photometric properties of rejected objects

Obj ID	α (J2000) (deg)	δ (J2000) (deg)	H_{160} (mag)	Colors C_1	C_2	$O_{ap.}$	O_{350}	S/N Y_{105}	J_{125}	JH_{140}	H_{160}	$z_{phot.}$ peak	z_{prior}	p_l/p_h	Reason of rejection
$z \sim 10$ candidates															
0807+3606-406	121.854693	36.100561	25.4	1.3 ± 0.3	0.6 ± 0.2	-0.3	-3.2	0.9	3.3	6.6	9.3	9.3	3.1	2.28	z_{prior}
0834+5238-575	128.508154	52.632111	26.3	2.0 ± 0.8	0.9 ± 0.3	0.5	0.4	0.9	1.3	4.0	7.5	7.0	3.6	2.16	vis
0851+4240-465	132.729208	42.670074	24.8	1.7 ± 0.5	0.6 ± 0.2	1.0	1.2	0.9	2.2	6.5	10.5	10.1	3.4	0.95	z_{prior}
0948+5757-185	147.048362	57.949351	25.4	2.1 ± 0.9	0.8 ± 0.2	0.4	-0.0	1.3	1.2	5.8	10.0	7.2	3.9	0.53	z_{prior}
0953+5153-1073	148.299729	51.877393	26.1	1.4 ± 0.6	0.6 ± 0.3	1.1	1.0	1.0	2.0	4.5	6.5	7.0	2.8	5.45	z_{prior}
0956+2848-401	149.093549	28.792157	26.2	1.4 ± 0.5	0.7 ± 0.3	1.0	1.0	0.9	2.1	4.5	7.6	9.9	3.1	1.41	z_{prior}
1136+0747-805	173.930982	7.777363	25.8	2.2 ± 1.1	0.8 ± 0.3	0.7	1.4	0.8	1.0	3.5	7.3	10.3	2.8	1.09	vis
1152+5433-109	177.928053	54.574866	25.8	1.4 ± 0.5	0.6 ± 0.2	-0.1	1.1	1.3	2.2	5.5	7.4	7.0	3.0	2.55	z_{prior}
1218+3008-265	184.563250	30.136829	24.4	1.8 ± 0.2	0.7 ± 0.1	-0.3	0.2	0.7	4.4	13.1	21.4	10.1	3.5	0.47	z_{prior}
1619+2541-760	244.807436	25.686392	26.5	2.2 ± 1.0	0.9 ± 0.3	-1.4	-1.0	1.0	1.1	3.5	7.3	7.5	3.9	0.11	vis
1738+1839-581	264.400431	18.664927	27.0	1.5 ± 0.7	0.6 ± 0.3	0.7	1.3	-0.3	1.7	3.8	6.1	9.9	3.2	1.49	vis
2134-0708-645†	323.562304	-7.120044	25.4	1.8 ± 0.8	0.5 ± 0.2	0.5	1.0	-0.2	1.4	5.7	6.9	10.0	10.4	0.12	z_{prior}
2229-0945-424	337.196149	-9.738446	26.4	1.8 ± 0.6	0.8 ± 0.3	-1.1	-0.4	-0.2	1.8	4.8	8.5	10.2	3.5	6.05	vis
2312-1423-353	347.931939	-14.404852	25.4	1.7 ± 0.5	1.0 ± 0.3	-0.2	-0.4	0.5	2.1	3.6	9.1	10.2	3.6	1.75	z_{prior}
$z \sim 9$ candidates															
0116+1425-442	19.034665	14.402626	24.4	1.8 ± 0.4	0.1 ± 0.1	0.2	-0.8	2.7	11.0	14.4	16.4	8.4	8.7	0.32	Y_{098}
0314-6712-1393	48.393390	-67.198000	26.5	1.8 ± 0.8	0.0 ± 0.3	0.8	0.7	1.3	3.6	6.1	5.6	8.4	2.0	0.87	z_{prior}
0337-0507-775	54.365817	-5.118763	25.0	1.8 ± 0.6	-0.0 ± 0.1	3.0	1.2	1.9	6.1	13.1	10.8	7.7	2.0	1.05	$O_{ap.}$
0554-6005-812	88.383324	-60.080277	26.8	> 1.9	-0.1 ± 0.3	0.7	1.1	0.1	3.2	6.8	4.9	9.2	2.1	0.38	z_{prior}
0751+2917-410	117.723475	29.287342	25.1	> 3.0	-0.0 ± 0.1	0.0	-4.7	0.0	11.9	12.6	10.7	9.2	8.8	0.17	vis
0751+2917-499	117.717853	29.288468	25.4	> 2.4	0.1 ± 0.2	0.0	0.9	0.7	4.8	7.8	7.5	9.0	8.9	0.05	Y_{098}
0952+5150-162	148.066856	51.817542	25.4	1.6 ± 0.5	0.1 ± 0.2	0.6	0.4	2.3	4.4	9.4	8.4	7.7	2.0	0.79	z_{prior}
1017-2052-119	154.367086	-20.858955	24.9	1.6 ± 0.6	0.1 ± 0.2	0.1	-0.6	2.0	4.4	9.5	9.0	7.4	2.0	1.10	z_{prior}
1104+2813-156	165.968967	28.198873	24.9	1.7 ± 0.5	0.0 ± 0.1	0.9	-0.3	2.3	5.6	11.5	10.9	7.5	2.0	1.07	z_{prior}
1152+5433-577	177.915777	54.541200	26.4	> 1.5	0.1 ± 0.3	-0.4	-0.4	0.1	3.9	6.2	5.0	8.7	8.7	0.08	vis
1152+5433-664	177.922295	54.541692	26.4	> 1.5	-0.1 ± 0.3	0.3	-0.1	-3.5	3.7	6.1	4.4	9.0	9.0	0.01	vis
1438-0142-939	219.459857	-1.683573	26.6	> 2.8	-0.9 ± 0.3	0.1	-0.5	0.3	0.1	10.5	4.2	10.5	2.0	1.14	vis
1442-0212-600	220.555169	-2.177198	25.6	> 2.2	0.2 ± 0.2	0.9	0.8	0.9	4.9	7.9	6.8	8.8	8.8	0.22	z_{flat}
1520-2501-228	230.076333	-25.013525	24.2	1.7 ± 0.3	0.2 ± 0.1	0.6	-0.1	3.1	8.0	14.1	16.4	7.5	8.6	0.72	z_{flat}
2008-6610-77	302.024097	-66.165779	25.7	> 2.4	0.1 ± 0.2	0.2	-0.6	0.8	8.7	8.6	8.4	8.9	8.9	0.34	z_{flat}
2229-0945-755	337.194543	-9.768108	26.3	2.1 ± 1.0	-0.2 ± 0.2	0.7	0.0	1.1	7.8	8.9	7.0	8.8	8.8	0.02	vis
2312-1423-763	347.926274	-14.380445	26.1	> 2.1	0.1 ± 0.2	-0.2	1.0	-0.8	3.2	6.6	7.0	10.1	8.8	0.61	z_{prior}

Note. — Same as Table 2, but for those color selected objects rejected by either of followings. Reason of rejection—vis: Visual inspection. z_{flat} : Photometric redshifts with a flat prior show inconsistent results with color-cut criteria and/or the peak of high- z probability is not sufficient compared to the low- z one ($p_{low}/p_{high} > 0.2$). z_{prior} : Same as z_{flat} but for photometric redshifts with a custom prior (Section 2.5.3). $O_{ap.}$: Excess of O_{350} flux ($S/N > 1.5$) in a small aperture (radius of $0''.16$). Y_{098} : Follow-up study rejects the high- z possibility (Livermore et al. 2018). †: Candidates selected in C16.

REFERENCES

- Anderson, J. 2014, The Impact of x-CTE in the WFC3/UVIS detector on Astrometry, Tech. rep.
- Atek, H., Richard, J., Kneib, J.-P., & Schaerer, D. 2018, ArXiv e-prints, arXiv:1803.09747
- Atek, H., Richard, J., Jauzac, M., et al. 2015, *ApJ*, 814, doi:10.1088/0004-637X/814/1/69
- Barone-Nugent, R. L., Trenti, M., Wyithe, J. S. B., et al. 2014, *ApJ*, 793, 17
- Behroozi, P. S., Wechsler, R. H., & Conroy, C. 2013, *ApJ*, 770, 57
- Benítez, N. 2000, *ApJ*, 536, 571
- Bernard, S. R., Carrasco, D., Trenti, M., et al. 2016, *ApJ*, 827, 76
- Bertin, E., & Arnouts, S. 1996, *A&AS*, 117, 393
- Birnboim, Y., & Dekel, A. 2003, *MNRAS*, 345, 349
- Bouwens, R. J., Illingworth, G. D., Oesch, P. A., et al. 2017, *ApJ*, 843, 41
- . 2015a, *ApJ*, 811, 140
- . 2014, *ApJ*, 793, 115
- . 2015b, *ApJ*, 803, 34
- Bouwens, R. J., Aravena, M., Decarli, R., et al. 2016, *ApJ*, 833, 72
- Bradley, L. D., Trenti, M., Oesch, P. A., et al. 2012, *ApJ*, 760, 108
- Brammer, G., Pirzkal, N., McCullough, P., & MacKenty, J. 2014, Time-varying Excess Earth-glow Backgrounds in the WFC3/IR Channel, Tech. rep.
- Brammer, G. B., van Dokkum, P. G., & Coppi, P. 2008, *ApJ*, 686, 1503
- Brinchmann, J., Inami, H., Bacon, R., et al. 2017, *A&A*, 608, A3
- Bruzual, G., & Charlot, S. 2003, *MNRAS*, 344, 1000
- Calvi, V., Trenti, M., Stiavelli, M., et al. 2016, *ApJ*, 817, 120
- Calzetti, D., Armus, L., Bohlin, R. C., et al. 2000, *ApJ*, 533, 682
- Cardelli, J. A., Clayton, G. C., & Mathis, J. S. 1989, *ApJ*, 345, 245
- Carrasco, D., Trenti, M., Mutch, S., & Oesch, P. 2018, ArXiv e-prints, arXiv:1805.08985
- Casertano, S., de Mello, D., Dickinson, M., et al. 2000, *AJ*, 120, 2747
- Clay, S. J., Thomas, P. A., Wilkins, S. M., & Henriques, B. M. B. 2015, *MNRAS*, 451, 2692
- Coe, D., Benítez, N., Sánchez, S. F., et al. 2006, *AJ*, 132, 926
- Coe, D., Zitrin, A., Carrasco, M., et al. 2013, *ApJ*, 762, 32
- Cowley, W. I., Baugh, C. M., Cole, S., Frenk, C. S., & Lacey, C. G. 2018, *MNRAS*, 474, 2352
- Curtis-Lake, E., McLure, R. J., Dunlop, J. S., et al. 2016, *MNRAS*, 457, 440
- Ellis, R. S., McLure, R. J., Dunlop, J. S., et al. 2013, *ApJ*, 763, L7
- Erb, D. K., Pettini, M., Shapley, A. E., et al. 2010, *ApJ*, 719, 1168
- Faber, S. M., & Jackson, R. E. 1976, *ApJ*, 204, 668
- Fan, X., Carilli, C. L., & Keating, B. 2006, *ARA&A*, 44, 415
- Fan, X., White, R. L., Davis, M., et al. 2000, *AJ*, 120, 1167
- Fan, X., Strauss, M. A., Schneider, D. P., et al. 2003, *AJ*, 125, 1649
- Finkelstein, S. L., Ryan, Jr., R. E., Papovich, C., et al. 2015, *ApJ*, 810, 71
- Finlator, K., Oppenheimer, B. D., & Davé, R. 2011, *MNRAS*, 410, 1703
- Foreman-Mackey, D., Hogg, D. W., Lang, D., & Goodman, J. 2013, *PASP*, 125, 306
- Gehrels, N. 1986, *ApJ*, 303, 336
- Grazian, A., Castellano, M., Fontana, A., et al. 2012, *A&A*, 547, A51
- Grogin, N. A., Kocevski, D. D., Faber, S. M., et al. 2011, *ApJS*, 197, 35
- Harikane, Y., Ouchi, M., Ono, Y., et al. 2018, *PASJ*, 70, S11
- Holwerda, B. W., Bouwens, R., Oesch, P., et al. 2015, *ApJ*, 808, 6
- Holwerda, B. W., Trenti, M., Clarkson, W., et al. 2014, *ApJ*, 788, 77
- Ilbert, O., Capak, P., Salvato, M., et al. 2009, *ApJ*, 690, 1236
- Ishigaki, M., Kawamata, R., Ouchi, M., et al. 2015, *ApJ*, 799, 12
- . 2018, *ApJ*, 854, 73
- Ishigaki, M., Ouchi, M., & Harikane, Y. 2016, *ApJ*, 822, 5
- Jaacks, J., Choi, J.-H., Nagamine, K., Thompson, R., & Varghese, S. 2012, *MNRAS*, 420, 1606
- Kalirai, J. 2018, *Contemporary Physics*, 59, 251
- Kawamata, R., Ishigaki, M., Shimasaku, K., Oguri, M., & Ouchi, M. 2015, *ApJ*, 804, 103
- Kawamata, R., Ishigaki, M., Shimasaku, K., et al. 2017, ArXiv e-prints, arXiv:1710.07301
- . 2018, *ApJ*, 855, 4
- Kelson, D. D., Benson, A. J., & Abramson, L. E. 2016, ArXiv e-prints, arXiv:1610.06566
- Koekemoer, A. M., Faber, S. M., Ferguson, H. C., et al. 2011, *ApJS*, 197, 36
- Konno, A., Ouchi, M., Ono, Y., et al. 2014, *ApJ*, 797, 16
- Kriek, M., van Dokkum, P. G., Labbé, I., et al. 2009, *ApJ*, 700, 221
- Livermore, R. C., Finkelstein, S. L., & Lotz, J. M. 2017, *ApJ*, 835, 113
- Livermore, R. C., Trenti, M., Bradley, L. D., et al. 2018, *ApJ*, 861, L17
- Madau, P., & Dickinson, M. 2014, *ARA&A*, 52, 415
- Maraston, C. 2005, *MNRAS*, 362, 799
- Mason, C. A., Trenti, M., & Treu, T. 2015a, *ApJ*, 813, 21
- Mason, C. A., Treu, T., Dijkstra, M., et al. 2018a, *ApJ*, 856, 2
- Mason, C. A., Treu, T., Schmidt, K. B., et al. 2015b, *ApJ*, 805, 79
- Mason, C. A., Treu, T., de Barros, S., et al. 2018b, *ApJ*, 857, L11
- McLeod, D. J., McLure, R. J., & Dunlop, J. S. 2016, *MNRAS*, 459, 3812
- McLure, R. J., Dunlop, J. S., Bowler, R. A. A., et al. 2013, *MNRAS*, 432, 2696
- Merlin, E., Bourne, N., Castellano, M., et al. 2016, *A&A*, 595, A97
- Muñoz, J. A., & Loeb, A. 2008, *MNRAS*, 385, 2175
- Noeske, K., Baggett, S., Bushouse, H., et al. 2012, WFC3 UVIS Charge Transfer Efficiency October 2009 to October 2011, Tech. rep.
- Oesch, P. A., Bouwens, R. J., Illingworth, G. D., Labbé, I., & Stefanon, M. 2018, *ApJ*, 855, 105
- Oesch, P. A., Stiavelli, M., Carollo, C. M., et al. 2007, *ApJ*, 671, 1212
- Oesch, P. A., Bouwens, R. J., Carollo, C. M., et al. 2010, *ApJ*, 709, L21
- Oesch, P. A., Bouwens, R. J., Illingworth, G. D., et al. 2012, *ApJ*, 745, 110
- . 2013, *ApJ*, 773, 75
- Oesch, P. A., Brammer, G., van Dokkum, P. G., et al. 2016, *ApJ*, 819, 129
- Oke, J. B., & Gunn, J. E. 1983, *ApJ*, 266, 713
- Ono, Y., Ouchi, M., Curtis-Lake, E., et al. 2013, *ApJ*, 777, 155
- Ono, Y., Ouchi, M., Harikane, Y., et al. 2018, *PASJ*, 70, S10
- Ouchi, M., Shimasaku, K., Furusawa, H., et al. 2010, *ApJ*, 723, 869
- Peng, Y.-j., Lilly, S. J., Kovač, K., et al. 2010, *ApJ*, 721, 193
- Pirzkal, N., Rothberg, B., Ryan, R., et al. 2013, *ApJ*, 775, 11
- Planck Collaboration, Ade, P. A. R., Aghanim, N., et al. 2014, *A&A*, 571, A16
- Ren, K., Trenti, M., & Mutch, S. J. 2018, *ApJ*, 856, 81
- Robertson, B. E., Ellis, R. S., Dunlop, J. S., McLure, R. J., & Stark, D. P. 2010, *Nature*, 468, 49
- Salmon, B., Coe, D., Bradley, L., et al. 2017, ArXiv e-prints, arXiv:1710.08930
- . 2018, ArXiv e-prints, arXiv:1801.03103
- Salpeter, E. E. 1955, *ApJ*, 121, 161
- Salvato, M., Ilbert, O., & Hoyle, B. 2018, *Nature Astronomy*, arXiv:1805.12574
- Schenker, M. A., Robertson, B. E., Ellis, R. S., et al. 2013, *ApJ*, 768, 196
- Schlafly, E. F., & Finkbeiner, D. P. 2011, *ApJ*, 737, 103
- Schlegel, D. J., Finkbeiner, D. P., & Davis, M. 1998, *ApJ*, 500, 525
- Schmidt, K. B., Treu, T., Trenti, M., et al. 2014, *ApJ*, 786, 57
- Sersic, J. L. 1968, *Atlas de galaxies australes*
- Shibuya, T., Ouchi, M., & Harikane, Y. 2015, *ApJS*, 219, 15
- Shull, J. M., Harness, A., Trenti, M., & Smith, B. D. 2012, *ApJ*, 747, 100
- Sobral, D., Matthee, J., Darvish, B., et al. 2015, *ApJ*, 808, 139
- Somerville, R. S., Lee, K., Ferguson, H. C., et al. 2004, *ApJ*, 600, L171
- Spergel, D., Gehrels, N., Baltay, C., et al. 2015, ArXiv e-prints, arXiv:1503.03757
- Stefanon, M., Labbé, I., Bouwens, R. J., et al. 2017, *ApJ*, 851, 43
- Stiavelli, M. 2009, *From First Light to Reionization: The End of the Dark Ages*
- Tacchella, S., Trenti, M., & Carollo, C. M. 2013, *ApJ*, 768, L37
- Totani, T., Kawai, N., Kosugi, G., et al. 2006, *PASJ*, 58, 485
- Trac, H., Cen, R., & Mansfield, P. 2015, *ApJ*, 813, 54
- Trenti, M., Perna, R., Levesque, E. M., Shull, J. M., & Stocke, J. T. 2012a, *ApJ*, 749, L38
- Trenti, M., & Stiavelli, M. 2008, *ApJ*, 676, 767
- Trenti, M., Stiavelli, M., Bouwens, R. J., et al. 2010, *ApJ*, 714, L202
- Trenti, M., Bradley, L. D., Stiavelli, M., et al. 2011, *ApJ*, 727, L39
- . 2012b, *ApJ*, 746, 55
- Treu, T., Schmidt, K. B., Trenti, M., Bradley, L. D., & Stiavelli, M. 2013, *ApJ*, 775, L29
- Treu, T., Trenti, M., Stiavelli, M., Auger, M. W., & Bradley, L. D. 2012, *ApJ*, 747, 27
- van Dokkum, P. G., Franx, M., Kelson, D. D., & Illingworth, G. D. 2001, *ApJ*, 553, L39
- Vulcani, B., Trenti, M., Calvi, V., et al. 2017, *ApJ*, 836, 239
- Wilkins, S. M., Bouwens, R. J., Oesch, P. A., et al. 2016, *MNRAS*, 455, 659
- Williams, C. C., Curtis-Lake, E., Hainline, K. N., et al. 2018, *ApJS*, 236, 33
- Woo, J., Dekel, A., Faber, S. M., et al. 2013, *MNRAS*, 428, 3306
- Yung, L. Y. A., Somerville, R. S., Finkelstein, S. L., Popping, G., & Davé, R. 2018, ArXiv e-prints, arXiv:1803.09761
- Zitrin, A., Labbé, I., Belli, S., et al. 2015, *ApJ*, 810, L12